## DISCLAIMER

# Final Technical Report (FTR)

## Cover Page

| | | |
|---|---|---|
| ***a.*** *Federal Agency* | Department of Energy | |
| ***b.*** *Award Number* | DE-EE0008999 (non-lab) | |
| ***c.*** *Project Title* | Polarimetry-Enhanced Imaging towards Autonomous Solar Field and Receiver Inspections | |
| ***d.*** *Recipient Organization* | Arizona State University | |
| ***e.*** *Project Period* | *Start:* 08/01/20 | *End:* 10/31/24 |
| ***f.*** *Principal Investigator (PI)* | Name: Yu Yao<br>Title: Associate Professor<br>Email address: yuyao@asu.edu<br>Phone number: 480-965-9208 | |
| ***g.*** *Business Contact (BC)* | Name: Heather Clark<br>Title: Executive Director Office of Research & Sponsored Projects Administration<br>Email address: Heather.Christina.Clark@asu.edu<br>Phone number: (480) 965-7874 | |
| ***h.*** *Certifying Official (if different from the PI or BC)* | Name:<br>Title<br>Email address<br>Phone number | |

*Signature of Certifying Official* *12/16/24* *Date*

*By signing this report, I certify to the best of my knowledge and belief that the report is true, complete, and accurate. I am aware that any false, fictitious, or fraudulent information, misrepresentations, half-truths, or the omission of any material fact, may subject me to criminal, civil or administrative penalties for fraud, false statements, false claims or otherwise. (U.S. Code Title 18, Section 1001, Section 287 and Title 31, Sections 3729-3730). I further understand and agree that the information contained in this report are material to Federal agency's funding decisions and I have any ongoing responsibility to promptly update the report within the time frames stated in the terms and conditions of the above referenced Award, to ensure that my responses remain accurate and complete.*

1. **Acknowledgement:** "This material is based upon work supported by the U.S. Department of Energy's Office of Energy Efficiency and Renewable Energy (EERE) Solar Energy Technologies Office (SETO) under the FOA 0002064 Award Number DE-EE0008999."



## 3. Executive Summary:

The main objective of this project is to apply polarimetric imaging techniques to CSP field inspections and develop polarimetric drone cameras (via integrating polarimetric imagers onto drones) for autonomous field inspection in CSP plants. To achieve this goal, we accomplished the following tasks in the project.

1) We have completed the fabrication and integration of chip-integrated a dual-color polarimetric imaging sensor. The device characterization results show root-mean-square (RMS) measurement errors for Stokes parameters $S_1$ $S_2$ and $S_3$ are all less than 0.02. We have performed outdoor polarimetric imaging with the demonstrated handheld camera.
2) We have completed a polarimetric imaging drone with a frame rate of 20fps and polarization measurement error <2% (for the degree of linear polarization (DOLP) and angle of polarization (AOP)) and use it for field tests in Sandia National Solar Thermal Test Facility (NSTTF). We have improved the system performance based on the feedback from the field tests.
3) We have performed polarimetry imaging of heliostat mirrors at Sandia's NSTTF in different settings with both a handheld polarimetric imaging sensor (phase I) and a UAV-integrated polarimetric imaging sensor in multiple field tests. We have applied polarimetric imaging analysis algorithms on CSP mirror images taken at Sandia National Solar Thermal Test Facility (NSTTF), and the results show obvious improvement in image contrast for mirror edges, corners and cracks for mirror facets. The success rates are >90%. We have collected polarization images of the heliostats which are suitable for optical error evaluation based on the UFACET method. We have developed the method for estimating the optical error of heliostat mirror facets based on polarization images and proved the feasibility of using polarimetric imaging for quick evaluation of heliostat optical errors based on optical models developed for heliostats. It is particularly important for the CSP plants, where the heliostat canting,

tracking and aiming may be far less than ideal, to ultimately reduce optical loss due to canting and tracking errors and increase energy efficiency up to > 1% (best-effort performance[1]).

4) We developed a rapid, cost-effective, user-friendly and non-intrusive Polarimetric Imaging-based mirror soiling detection (PIMS) method. The PIMS imaging device is very compact and can be integrated into an unmanned aerial vehicle (UAV) for single-shot measurement of large area measurement on Heliostat mirrors for fast soiling detection without labor-intensive inspection on each facet with a reflectometer individually. With the skylight as natural light source, we developed a methodology to correlate the Degree of Linear Polarization (DoLP) image of mirrors to their soiling levels using an experimentally calibrated model based on Mie Scattering Theory and Monte-Carlo simulation. For field deployment of the PIMS method, minimal pre-installation is required, and the field operation is not interrupted by the UAV imaging process. The autonomous detection of soiling conditions and defects can greatly improve the efficiency in scheduling heliostat washing and repair, and as a result, can potentially increase the solar-weighted heliostat reflectance and the collector optical efficiency by up to 4%.
5) We have also shown that polarimetry imaging provides a significant enhancement for the detection of scratches and areas with missing black paint. The ASU team has set up a theoretical model for a better understanding of the polarimetry imaging results of the receiver tube. The results show good agreement with experimental results and suggest that visible polarimetric imaging with sunlight and skylight can provide robust imaging contrast for the detection of receiver tube defects, such as missing black paints, scratches, deformation (e.g., tube bending), etc.

[1] Here we consider the fact that the optical errors account for >1% energy loss in CSP plants, according to DE-FOA-0002064 (page 47)

## 4. Table of Contents



## 5. Background

During the typical operation of a Concentrating Solar Power (CSP) plant, a large portion of the energy (~45%) can be lost due to various imperfect conditions, such as blocking, shading, mirror soiling, tracking and canting errors, etc. It is necessary to develop efficient and effective field inspection technology to optically survey and characterize a CSP field, which can be used as an input for autonomous control, maintenance scheduling and spot repair whenever necessary to maximize the overall efficiency of the plant [1]. Currently, conventional visible and thermal imaging systems are being used for field inspection of CSP fields; however, there are various limitations of the state-of-art technology in terms of accuracy, speed and capability:

1) Standard, visible, high-resolution drone cameras with standard edge detection techniques have been used to detect heliostat edges and corners for optical error measurements on the heliostats. However, the edges can be difficult to find automatically when there is low contrast between the mirror image and the background, *e.g.,* when the mirror image and background are both blue sky.
2) The autonomous detection of mirror defects and soiling conditions remains elusive, mainly due to low contrast in images taken by conventional cameras. Mirror soiling greatly affects collection efficiency, but its cleaning is currently determined by manual measurement using hand-held reflectometers that are slow and only cover a very small portion of the mirror surface.
3) Currently, some commercial plant operators use drone cameras to inspect the receiver surface for cracks, paint peeling off and other damage. They also use infrared (thermal) cameras to monitor receiver temperature to prevent catastrophic failure due to hot spots. However, the sensitivity of the visible imaging technique is limited by the imaging contrast, while the thermal imaging technique suffers from spatial resolution and inaccurate temperature measurement (due to varying emissivity values at

different temperatures of the receiver surface).
The Sandia team has been working on developing optical error detection methods for CSP collectors with drone cameras. They have developed advanced algorithms to improve detection probability and accuracy. Yet, the method based on conventional cameras may require capturing multiple images to improve the detection accuracy. Processing these high-resolution images can be time-consuming, making it nearly impossible to realize real-time or near-real-time processing.

## 6. Project Objectives

We aim to apply polarimetric imaging for CSP collector and receiver inspection and develop polarimetric drone cameras (via integrating polarimetric imagers onto drones) for autonomous field inspection in CSP plants.

In this project, we plan to explore the application of the proposed systems to:
(1) Develop techniques to detect edges and corners of heliostats and facets. This will address the serious technical challenges that prevent current camera-based optical inspection tools from fast and reliable detection. Expected outcome: polarimetric imaging can provide edge/corner detection solutions for current optical inspection tools, and improve the success rate of detection to > 95% and the detection speed to>1 heliostat/min.
(2) Develop techniques to monitor mirror soiling and quantitatively report solar-weighted reflectance. This will fill the technology gap to perform such measurements. Expected outcome: This technique will increase heliostat coverage area at accuracies (error <2%) comparable to commercial reflectometers with high inspection speed >1 heliostat/min, thus enabling timely mirror cleaning protocols.
(3) Develop techniques to inspect and monitor receivers for hot spots, tube defects, and paint degradation. Currently, both IR and visible cameras are used to perform these inspections, but the detection accuracy is often limited by low image contrast for defects and thus not suitable for autonomous detection. Expected outcome: Expected outcome: Our polarimetric imaging systems can potentially serve to detect in both visible and IR ranges and provide both temperature and polarization-based inspection. This may enable accurate detection (>95%) of small scratches, cracks, and other defects to avoid major damages and failures.

| TWP Item Number (Tasks, Subtaks, and Milestones) | Item Description |
|---|---|
| **T-1** | **Demonstrate polarimetric imaging systems for autonomous detection** |
| ST-1.1 | **Demonstrate a portable full-stokes polarimetric visible imaging sensor (FSPvis)** |
| M (1.1.1) | A portable linear polarization image sensor with polarization measurement error <3% for Degree of Linear Polarization (DOLP) and Angle of Polarization (AOP) |

| | |
|---|---|
| GNG (1.1.3) | A portable FSPvis with speed >5fps and polarization measurement error <2% for Degree of Polarization (DOP) and AOP |
| ST-1.2 | **Fabricate on-chip integrated full-stokes polarimetric imaging sensor chips** |
| M (1.1.2) | Integrate polarization filters by EBL over millimeter scale on CMOS image sensors and IR FPAs (alignment error: lateral <200 nm, structure dimension deviation <10 nm ) |
| M (2.1.3) | Integrate polarization filters by NIL over centimeter-scale on CMOS image sensors and IR FPAs (alignment error: lateral <200 nm lateral, rotational <0.05˚ ) |
| M (3.1.1) | High throughput fabrication of full-stokes polarimetric imaging sensors (NanoImprint Lithography speed <5 min/cm$^2$) |
| ST-1.3 | **Demonstrate a portable infrared full-stokes polarimetric imaging sensor (FSPir)** |
| GNG(1.1.4) | A portable FSPir with polarization measurement error <3% for DOPand AOP |
| ST-1.4 | **Integrate FSPvis on UAVs for autonomous detection in the outdoor environment** |
| GNG(2.1.2) | An FSPvis integrated into UAV automatically takes images outdoors (polarization measurement errors <3% for DOP and AOP in wind speed <10mph) |
| ST-1.5 | **Integrate FSPir for autonomous detection in the outdoor environment** |
| GNG(2.1.4) | An FSPir integrated into a UAV automatically takes images outdoors (polarization measurement errors <5% for DOP and AOP in wind speed <10mph) |
| ST-1.6 | **Evaluate and minimize the impact of windy conditions on polarimetric imaging sensors (wind speed 0-10 mph)** |
| M (2.1.1) | Minimize the impact of wind on UAV polarimetric imaging system to achieve measurement error <3% in wind (speed 10 mph) |
| EOP(3.1.2) | FSPvis (>15fps, DOP and AOP error <3%) and FSPir (>5fps, DOP and AOP error <5%) integrated on UAVs for autonomous detection in CSP plants. |
| **T-2** | **Autonomous detection of CSP heliostats optical errors and mirror defects** |
| ST-2.1 | **Theoretical modeling for CSP mirror edge, corner and defect detection** |
| M (1.2.1) | Algorithm for autonomous polarimetric detection of CSP mirror edges and corners |

| | |
|---|---|
| M (1.2.2) | Algorithm for autonomous polarimetric detection of CSP mirror scratches and cracks |
| ST-2.2 | **Perform autonomous detection of mirror edges, corners, and defects in the outdoor environment** |
| M(2.2.1) | Autonomous detection of mirror edges and corners with success rate >90% |
| M(2.2.2) | Autonomous detection of mirror scratches and cracks (length > 2cm, width > 1 mm) with success rate >90% |
| M(2.2.5) | Minimize the impact of the windy conditions to achieve high success rates of>85% for detection of mirror edge/corner and defects in wind speed < 10 mph. |
| ST-2.3 | **Perform field test in CSP plant of mirror edge/corner and defects and improve system/methodology based on field test results** |
| M (2.2.3) | Detection of CSP mirror edges and corners, scratches, and cracks in CSP plant with success rate >90% with portable polarimetric imaging sensors |
| M(2.2.4) | Accuracy of optical error valuation based on measurement results of CSP heliostats test modules with pre-defined optical errors. |
| GNG(2.2.6) | Detection of CSP mirror edges and corners, scratches and cracks with drone-integrated polarimetric imaging sensors (human controlled) in CSP plant with success rate >90% |
| M(3.2.1) | Autonomous detection of CSP mirror edges and corners with success rate>90% (>85% in wind speed 10 mph), speed 1 mirror/min |
| M(3.2.2) | Autonomous detection of CSP mirror scratches and cracks (length >2 cm, width > 1mm) with success rate >90% (>85% in wind speed 10 mph), speed 1 mirror/min |
| EOP-3.2.3 | Autonomous monitoring of collector fields to evaluate optical error, facilitate tracking accuracy, and inspect mirror defects with high speed (1 mirror/min) and success rate (>90%) |
| **T-3** | **Investigate the benefits and feasibility of applying polarimetric imaging to monitor mirror soiling condition** |
| ST-3.1 | **Collect mirror soiling patterns and dust samples from different CSP plants across the United States.** |
| M (1.3.1) | Samples of soiled CSP mirrors and dust samples from different CSP plants |
| ST-3.2 | **Investigate the feasibility of applying polarimetric imaging to monitor mirror soiling conditions by combining theoretical analysis and experimental study** |

| | |
|---|---|
| M (1.3.2) | Simulation results of sunlight polarization state when scattered off different sand particles (size 0.086-2 mm) on mirrors. Different sun positions (from sunrise to sunset) and light incident angle (complete angle range scan with 2-degree step size) will be considered. |
| GNG(2.3.1) | Experimental and simulation results of sunlight polarization state scattered off mirrors with various dust samples (obtained in ST-3.1, sand particle size distribution will be considered) at different soiling conditions to evaluate the accuracy and feasibility of detecting mirror soiling condition via polarimetric imaging |
| ST-3.3 | **Perform outdoor tests for mirror soiling condition monitoring and improve system/methodology based on experimental results** |
| M (3.3.1) | Detection of mirror soiling conditions outdoors using portable full-stokes polarimetric imaging sensor with accuracy (error <3%) |
| EOP(3.3.2) | Assessment of the benefits, technical feasibility and challenges of mirror soiling condition monitoring based on polarimetric imaging |
| **T-4** | **Investigate the feasibility of applying polarimetric imaging to monitor CSP receiver tubes** |
| ST-4.1 | **Collect information about receiver tube defects and the needs of CSP plants regarding receiver tube inspection** |
| M (1.4.1) | Samples of CSP receiver tubes+D13 with defects (scratches, cracks, etc) from CSP plants |
| ST-4.2 | **Investigate the feasibility of applying visible/ infrared polarimetric imaging to monitor receiver tube defects** |
| M (2.4.1) | Simulation results of the polarization states of infrared emission from receiver tubes with various types of defects and algorithm for receiver tube defects detection based on visible and infrared polarimetric images |
| GNG(2.4.2) | Polarimetric imaging analysis (visible and infrared images) of various types of defects on receiver tubes. |
| ST-4.3 | **Perform outdoor tests of autonomous receiver inspection outdoors and improve system/methodology based on experimental results** |
| M (3.4.1) | Detection of CSP receiver defects (scratches, cracks with length > 2cm and width > 1 mm) outdoors using drone-integrated full-stokes polarimetric imaging sensor with success rate >90% |
| EOP(3.4.2) | Assessment of the benefits, technical feasibility and challenges of CSP receiver tube condition monitoring based on polarimetric imaging |
| **T-5** | **Perform techno-economic analysis and develop a commercialization plan** |

| | |
|---|---|
| ST-5.1 | **Conduct a survey (including literature research, and discussion with relevant parties) about the potential benefits of full-stokes polarimetric imaging systems and drone-integrated polarimetric imaging sensors** |
| M(1.5.1) | A report on the value proposition of on-chip full stokes polarimetric imaging sensors and drone-integrated polarimetric imaging sensors in comparison with state-of-art technologies |
| ST-5.2 | **Conduct a survey (including literature research, discussion with workers in CSP plants and other relevant parties) about the potential benefits of polarimetry-based imaging for autonomous inspection of CSP plants** |
| M(1.5.2) | A report on the potential benefits (esp. estimated increase of energy efficiency and O&M cost reduction for MW CSP plants ) of autonomous detection of optical errors, mirror defects, soiling conditions, and receiver tube defects, as well as other functions discovered during the survey (literature research and conversation) |
| M(1.5.3) | A list of candidates' names for the advisory board from CSP and Sandia Labs and their letters of support. |
| ST-5.3 | **Reach out to potential industry partners to find out their interests in full-stokes polarimetric imaging sensors as well as drone-integrated polarimetric imaging systems** |
| M (3.5.2) | A list of industrial partners who will be involved in leading or participating in at least one of the following efforts: 1) scalable manufacturing of the polarimetric imaging devices, 2) integrating polarimetric imaging sensors on UAVs 3) applying polarimetric imaging sensors to various applications. |
| ST-5.4 | **Present field test results of autonomous detection of optical errors and mirror defects to CSP plants to find out their needs and cost expectations for autonomous inspection system** |
| M(2.5.1) | Feedback from the CSP plants on their interests in the inspection system and other expected functions |
| M(3.5.3) | Feedback from the CSP plants on the field test demo results and their interest in testing the system in their field |
| ST-5.5 | **Evaluate the benefits, costs, and risks in developing the proposed devices and systems based on experimental and field test results** |
| M(3.5.1) | A techno-economic analysis of the on-chip full stokes polarimetric imaging sensors and drone-integrated polarimetric imaging sensors |
| EOP(3.5.4) | A techno-economic analysis of the autonomous polarimetric imaging-based inspection system. |

| | |
|---|---|
| EOP(3.5.5) | A commercialization plan for the autonomous polarimetric imaging-based inspection system. |
| **T-6** | **Summary and final report** |

## 7. Project Results and Discussion

### Task 1: Demonstrate polarimetric imaging systems for autonomous detection

**Technical progress and outcomes:**

1. Complete a chip-integrated full-stokes polarimetric imaging sensor (total area: 2.4x3.6 $mm^2$; pixel number >60,000) with high measurement accuracy for all Stokes parameters for dual wavelengths (red and blue color). The average RMS errors for Stokes parameters $S_1$ $S_2$ and $S_3$ are all less than 2%, obtained by measurements in the lab setting. We completed the measurement at oblique incident angles and concluded that the demonstrated polarization imaging camera can maintain less than 5% error for all Stock parameters for a full angle range up to 40 degrees.
2. Finish the fabrication of an array of superpixels with the total area (2.7mmx2 mm) and integrate it with a thermal imaging system to make a portable mid-IR polarimetric imaging sensor. The achievable average RMS errors for Stokes parameters $S_1$ $S_2$ and $S_3$ are all less than 3%, obtained by measurements in the lab setting.
3. Demonstrate nanoimprint lithography (NIL) with reasonably good uniformity over an area of ~1x1 $cm^2$ based on a tri-layer nanoimprint method. Complete the modes for both layers with alignment markers (area: 5x6 $mm^2$, limited by the EBL writing time).
4. Complete an updated polarimetric imaging drone system (version 2) based on the feedback from the Sandia drone team and send it to Sandia. Based on the first field test, we identified some issues to solve before the next field test.
5. Finish the characterizations of CMOS imaging sensors to realize 3 polarimetric imaging sensors. The alignment error between the two metasurfaces is less than 200 nm and the SEM images show reasonably good uniformity. We have completed device calibration for full-stokes polarimetric imaging measurements and analyzed the measurement accuracy (errors for AOP and DOLP, DOCP are all <3%).
6. We have completed the second-generation polarimetric imaging drone system with improved performance and used it for a field test in Sandia.

***Develop full-stokes polarimetric imaging sensor***

We have completed chip-integrated full-stokes visible polarimetric CMOS imaging sensors and carried out device characterization in the lab (chip size: 2.4x3.6 $mm^2$, number

of pixels: ~60,000)[2]. Figure 1a shows a photo of the fabricated device. The polarization measurement is based on the spatial division method (Fig. 1b). Figure 1d shows a photo of the polarimetric camera with a zoom lens. This camera can provide a complete measurement of polarization states. Figure 1d shows the polarization images of a CP filter and a plastic cage. We have performed calibration and characterization of polarization measurement for all pixels and obtained high measurement accuracy for light incident onto the imaging sensor vertically (incident angle ~0 degrees, measurement error for all stokes parameters <2%). In this quarter, we achieved high measurement accuracy for both red and blue colors and also characterized the impact of the incident angle of light. The results are shown in Figure 2. The measurement results suggest that for measurements with high accuracy requirements (error <2%), such as mirror soiling measurement, the polarimetric imaging sensor FOA (full operation angle range) is about 20 degrees. For measurements that do not require high measurement accuracy, e.g., error <5% or <10%, the FOA can be up to 40 degrees or 60 degrees. Compared with our previous characterization of the Sony linear polarization camera, the full-stokes polarimetric imaging sensor we fabricated shows a larger operation angle range.

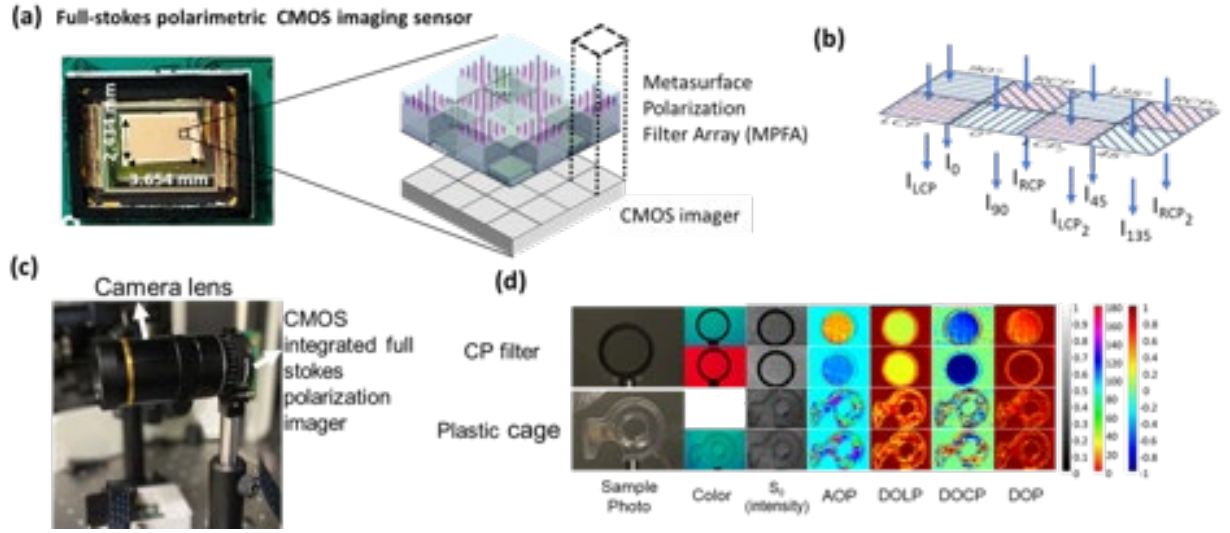


**Figure 1. Device design, fabrication, and imaging results of the full-stokes polarimetric imaging sensor.** (a) A photo of the fabricated imaging chip. Inset: a schematic of a microscale polarization filter array integrated onto a CMOS imaging sensor. (b) A schematic of the spatial division method. (c) A photo of the polarimetric CMOS imaging sensor. (d) Polarization images of a CP filter and a plastic cage were obtained with the imaging sensor. (AOP: angle of polarization, DOLP: degree of linear polarization; DOCP: degree of circular polarization; DOP: degree of polarization). Figure adapted with permission from reference [2]

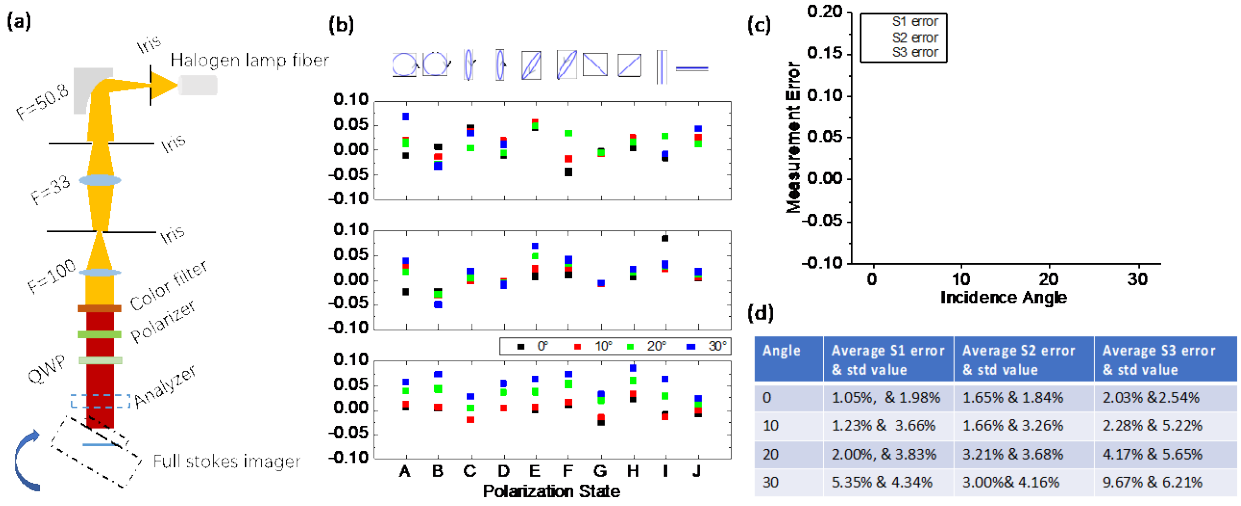


| Angle | Average S1 error & std value | Average S2 error & std value | Average S3 error & std value |
|---|---|---|---|
| 0 | 1.05%, & 1.98% | 1.65% & 1.84% | 2.03% &2.54% |
| 10 | 1.23% & 3.66% | 1.66% & 3.26% | 2.28% & 5.22% |
| 20 | 2.00%, & 3.83% | 3.21% & 3.68% | 4.17% & 5.65% |
| 30 | 5.35% & 4.34% | 3.00%& 4.16% | 9.67% & 6.21% |

Figure 2. Characterization results of CMOS polarimetric imaging sensor at different light incident angles. (a) A schematic of the characterization setup. (b) measurement error for different input light polarization states (A to J) at different incident angles from 0 to 30 degrees. Top panel: $S_1$; middle panel: $S_2$; Bottom panel: $S_3$. (c) Average measurement errors and error bars for the stokes parameters at different incident angles. (d) A table summary of the measurement results. Figure adapted with permission from reference[2]

## Develop nanoimprint lithography (NIL) large-scale high-throughput device fabrication

### *Scalable Manufacturing Process Overview*

We have developed a synergistic approach to co-design the multi-layered optical metasurfaces and their scalable NIL manufacturing process. Our exemplary polarimetric imaging system was a multilayered metasurface polarization filter array (MPFA) integrated into a CMOS imaging sensor (Fig. 3a). The MPFA consisted of over 43,000 superpixels, each having four linear polarization (LP) filters and four circular polarization (CP) filters to ensure accurate full-Stokes polarization measurement. The LP filters were based on vertically coupled double-layer gratings (VCDGs) with a high LP extinction ratio (LPER) over a broad wavelength range (Fig. 3b)[2]. The CP filters were based on multi-layered chiral metasurface structures[2, 3], consisting of a Si metasurface, a dielectric spacing layer, and VCDGs (Fig. 3c). Overall, the MPFA was formed by two vertically aligned, functional layers, i.e., the Si metasurface layer and the VCDG layer (Fig. 1a). In the Si metasurface layer, each superpixel had 4 blank pixels (no nanopatterns) and 4 pixels made of Si nanostructures. In the VCDG layer, the grating polarizers were present in all 8 pixels, oriented along 0°, 45°, 90° or 135° in the 4 LP filters and all along 90° in the 4 CP filters. To achieve a broadband coverage in visible (450 to 670 nm), two sets of CP filters (VCDGs + Si metasurface) were designed, one for green-wavelength operation (510 to 600 nm), and the other for blue (450 to 510 nm) and red wavelengths (600 to 670 nm). This design enabled a single-shot, full-Stokes polarimetric analysis and imaging (Fig. 1) over a broad bandwidth in visible wavelengths over 344,000 spatial points. As a proof-

of-concept demonstration, we fabricated the MPFA on a transparent silica substrate and then integrated it onto a commercial CMOS imaging sensor via polymer-assisted wafer bonding. The process can be readily modified to directly integrate the metasurface onto CMOS chips for wafer-scale production.

Previously, we have developed an EBL-based process to fabricate the MPFA[2], and demonstrated dual-color full-Stokes parameter detection with a high accuracy and a large field of view [2]. However, the fabrication process required extensive EBL writing time, repeated film deposition, lift-off and etching. Furthermore, the silicon oxide ($SiO_2$) spacer on top of the silicon (Si) metasurface displayed a rough surface (Ra = 28.3 nm) that resulted in rough Al gratings in the VCDGs and limited device LPER and CPER[2]. Fundamentally different from EBL lithography (Fig. 3e top, figures following orange arrows), NIL (Fig. 3e bottom, following green arrows) was utilized first as a high-throughput, high-resolution lithography technology to produce Si metasurface gratings, and then used as a three-dimensional surface topography replication process to print the VCDG grating scaffold in resists, which replaced the spacer layer in EBL fabrication. Thermal NIL was chosen for the Si metasurface fabrication for its simplicity, and UV-NIL was carried out for VCDGs by optically aligning a transparent mold to the Si metasurface and pressing the mold into a resist with an optical index comparable to $SiO_2$. Here Moiré patterns were created on both of the two NIL molds to achieve a high overlay accuracy over the patterned area. NIL, as a lithography approach, is hours faster than EBL when a mold is available, and its high throughput advantage can be further manifested when scaling to even bigger areas, reducing cost, and improving throughput in manufacturing. Moreover, the UV-NIL not only effectively produced the 3D VCDG scaffold, but also eliminated multiple manufacturing steps and planarized the resist despite underlying protruding topography from Si metasurface. As a result, such a new, simplified process simultaneously reduced processing complexity and improved the MPFA performance.

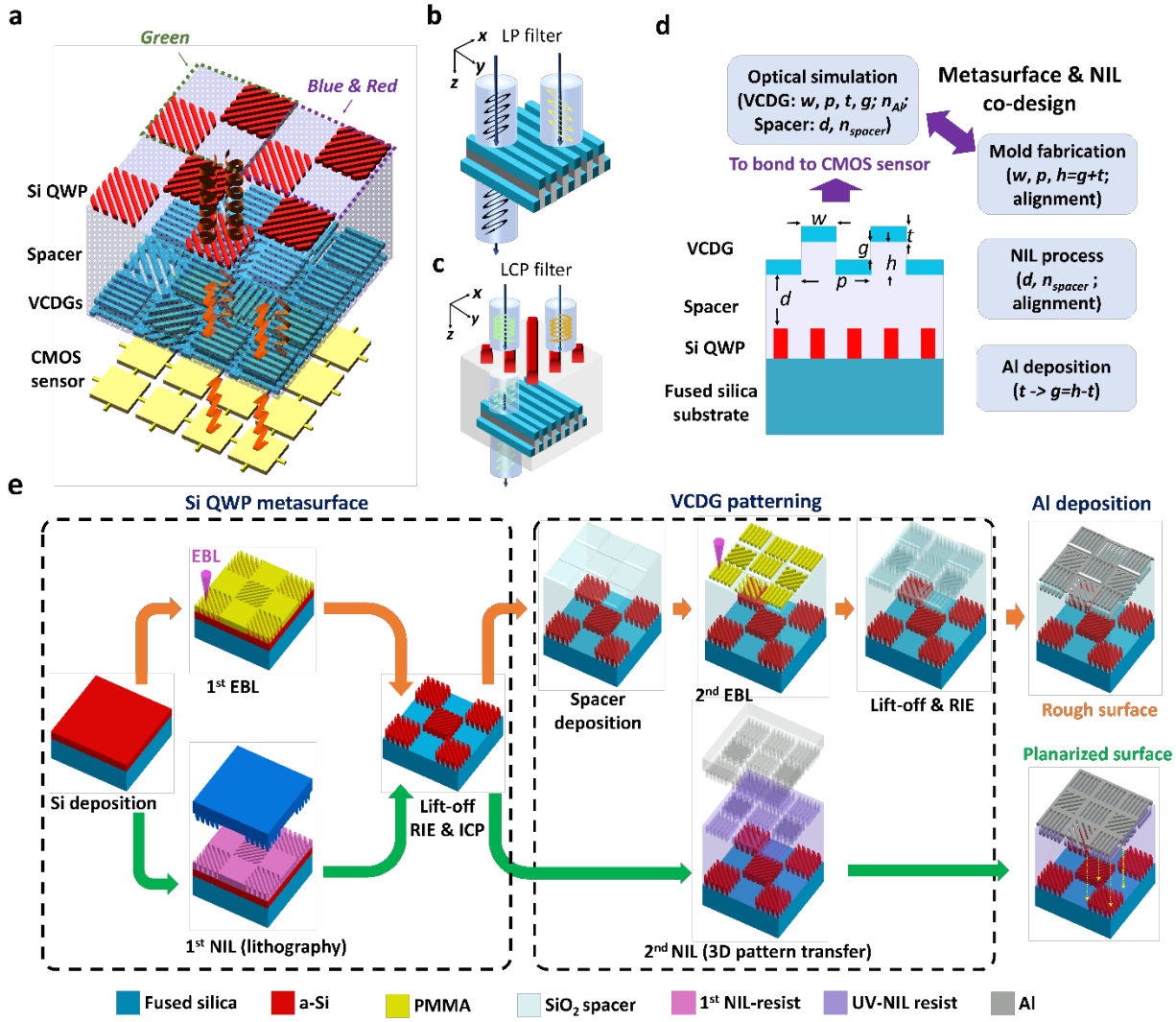


**Figure 3: Conceptual designs of scalable NIL manufacturing for multi-layer metasurfaces (MPFAs).** **a**, Illustration of integrating CMOS imager with broadband MPFAs consisting of a layer of Si metasurface as QWP and a layer of VCDGs as polarizers. Here two CP designs targeting green and blue/red spectra (indicated by arrows) are incorporated for the Si metasurface structures. **b**, Schematic of VCDG with transmission axes along the x-axis, electric field along the y-axis is thus blocked. **c**, Schematic of multi-layered CP filter transmitting LCP, RCP input is thus blocked. **d**, A co-design concept to produce the VCDGs on Si metasurface structures based on NIL. **e**, Schematics showing the EBL (top, following orange arrows) and NIL (bottom, following green arrows) based fabrication processes for MPFAs. Here a 1st NIL replaces EBL for the fabrication of Si metasurface, and a 2nd UV-NIL creates a nanostructured scaffold to be converted into VCDGs after Al evaporation. Figure adapted with permission from reference [4]

### *Imaging sensor integration and characterization*

The integrated multi-layer MPFAs were diced (7.2 mm × 5.6 mm) and bonded onto a commercial CMOS sensor (IMX477), as shown in Fig. 4a and 4b. The alignment was performed by aligning the cross-bar alignment markers of MPFAs to the four edges of CMOS sensors using a mask aligner. This alignment translational error was on the micrometer scale and the rotational error was about 0.02°, constrained by the lack of more accurate alignment marks (e.g. Moiré patterns) on the CMOS imaging sensors.

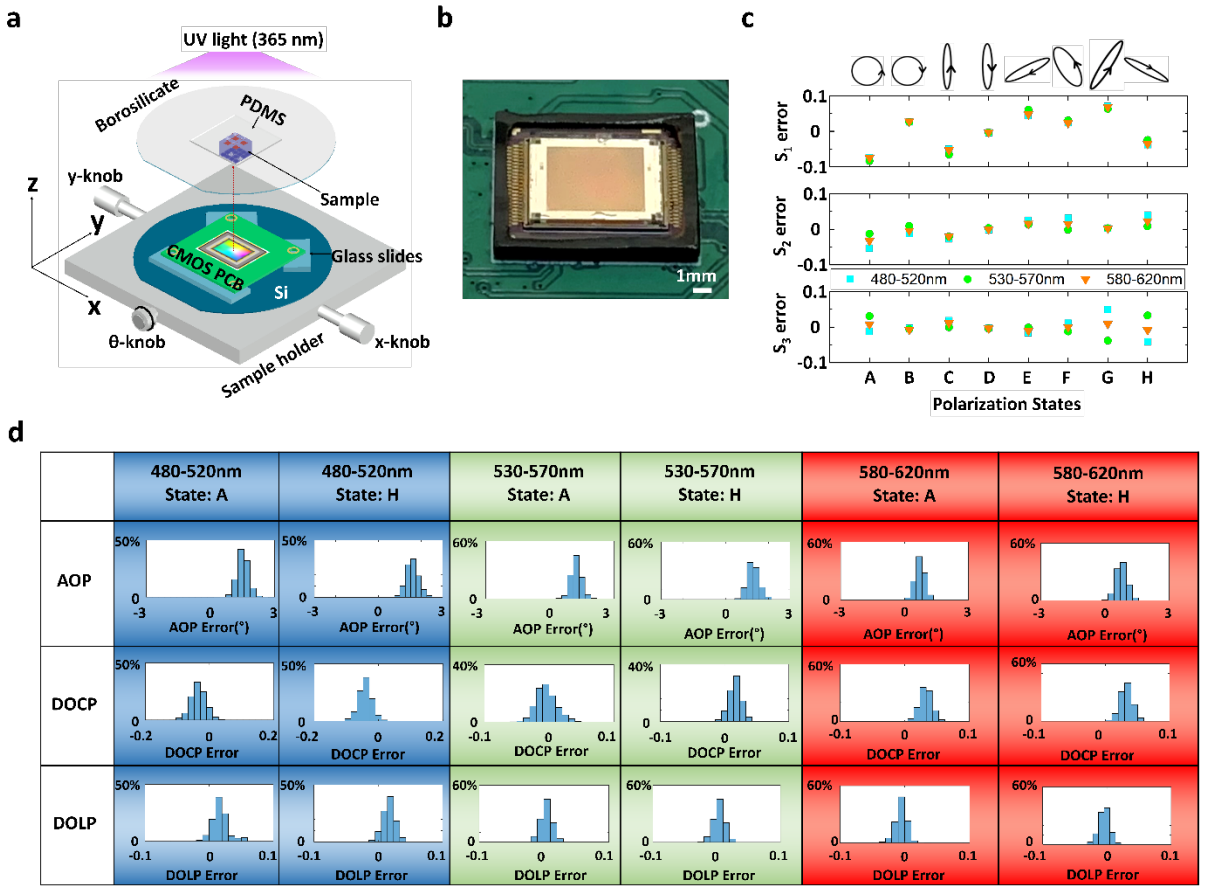


**Fig. 4. Multi-color full-Stokes polarization state detection using metasurface polarimetric imaging sensor. a**, Schematic of integrating metasurface polarization filter arrays onto CMOS imaging sensor. CMOS circuit board is firstly mounted onto the 3D rotation stage and leveled, then the metasurface array is aligned and bonded onto the board via a UV mask aligner. **b**, An optical image of the integrated metasurface polarimetric imaging sensor. **c**, Error analysis of multi-color full-Stokes parameter detection for eight polarization states (A to H). **d**, Multi-color AOP, DOCP, and DOLP detection error distributions of all metasurface pixels for polarization states A and H. X-axes represent the errors and Y axes represent the corresponding percentage of pixels. Figure adapted with permission from reference [4]

To further minimize these alignment errors, one can design the layouts of the CMOS imaging sensor and the metasurfaces with interferometric Moiré patterns, similar to what we demonstrated for high-accuracy alignment of multi-layer metasurface structures in the previous section. We characterized the bonded metasurface polarimetric imaging sensor (or Meta-PolarIm[2]) to determine its instrument matrix $A$ at different wavelength bands, i.e., 480-520 nm, 530-570 nm, and 580-620 nm, respectively. Thus, the Stokes parameters of any unknown input polarization state $S$ can be obtained using $S = A^{-1}I$, where $I$ represents the intensity vector obtained by all 8 subpixels in each superpixel of Meta-PolarIm[2]. We measured eight polarization states with Meta-PolarIm (Fig. 4c) to evaluate the polarization detection accuracy using a customized measurement setup [2]. The measurement error$\Delta S_i^j$ (i=1, 2, 3 for the Stokes parameters; j=1,2… 8 for the polarization states) was calculated by subtracting the measurement data from the

reference values obtained from theoretical calculation. The mean absolute error (MAE) for $S_1$, $S_2$, and $S_3$ is less than 5% at all color inputs. We also performed statistical analysis for the errors of all pixels in the imaging sensor, including measurement errors for the angle of polarization (AOP=$\frac{1}{2}\arctan\frac{S_2}{S_1}$), degree of circular polarization (DOCP=$S_3/S_0$) and degree of linear polarization (DOLP=$\sqrt{S_1^2+S_2^2}/S_0$) for eight polarization states over the three wavelength bands (Fig. 4d). The results suggested that 90% of the polarimetric imaging pixels have reasonably small measurement errors for DOLP (<3%), AOP (<1.8°) and DOCP (<2% for 530-570 nm and 580-620nm, <6% for 480-520 nm). Our results confirmed that the developed NIL-based nanomanufacturing method is suitable for producing multi-layer metasurface devices with reasonably good performance and uniformity across centimeter scales[4].

### *Integrate FSPvis on UAVs for autonomous detection*

Figure 5 shows the second-generation polarimetric imaging drone system we finally developed and deployed in the field test. The payload consists of the Polarization camera and Jetson Xavier NX as the microcontroller mounted onto a box (to protect it from outdoor elements and for a sturdy fix onto the gimbal) which is then mounted onto the gimbal as the payload. The payload weighs 0.5 Kgs(1.1lbs) which is much less than the maximum payload weight (3.7lbs) that the Gremsy T3 can withstand. The Jetson is mounted on the base with screws provided on the board and then covered with a case for protection against dust which could get into it while on flight. The camera is connected on the base mounted on pillars which gives us comfort to connect all the required accessories to jetson and to provide a light weight design. Mavlink provides full flight control and mission planning for any MAVLink enabled drone. Its primary goal is ease of use for professional users and developers. All the code is open-source source. The code runs on the Qt5 framework, which gives us more flexibility and more resources to enhance the GUI, to enable us to use several threads operating individually for better performance. The GUI has a Start Stream, Acquire Stream for saving the images and Stop Stream, a DoLP preview button. The software takes care of the exposure, with the inbuilt new Adaptive exposure feature, the GUI is able to detect the overexposed stream and bring down the overexposed pixels below the tolerance value that the user sets. It has the real time Mono8 camera feed as well as its real time DoLP Preview for better results and to check whether the images acquired could be used for inference. Using the 6 cores, we distribute the cores for real time DoLP computation as well as for real time streaming and saving, giving us an average of 18-22 fps, which is smooth and lag-free for us to correlate with the real time feed.

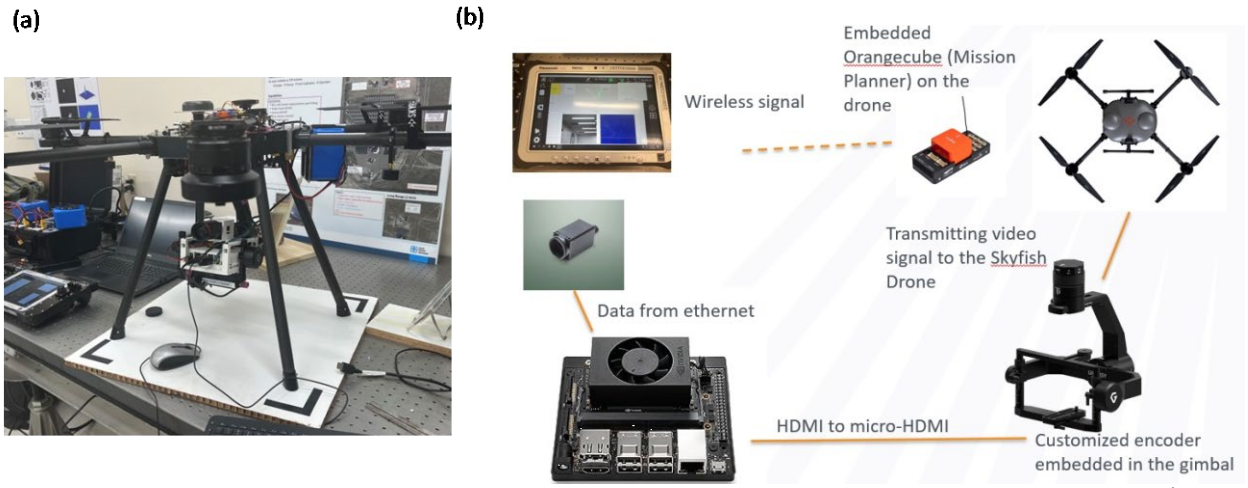


Figure 5: (a) a Photo of the updated payload integrated on the drone. (b) A schematic of the final 2nd generation polarimetric imaging drone.

**Improvements in the new GUI system**

The primary improvement is in the speed of the camera feed, which is now an average of 22 fps, which is 50% more improvement from the previous version. The GUI uses bigger buttons and wide aspect windows for better visibility. The stream is in full resolution (5.0 MP, 2448 x 2048 px), while giving a higher performance than previous versions. There is a dedicated Textbox, which is a separate thread used to display the background status of the GUI, such as saving and target brightness and other variables as text messages. The GUI has animations in buttons and it highlights, for example the Acquire Stream turns on/glows if the saving is initiated. The GUI has a separate thread for reading the serial messages as mavlink packets through the mavlink protocol which reads the value of the PWM of the RC controller and decides the actions. There are dedicated channels for triggering the Acquire frame button and Preview DoLP button.

Figure 6. A screen shot of the new GUI interface.

## Task 2: Autonomous detection of CSP heliostat optical errors and mirror defects

Technical progress and outcomes:

1. We have collected polarimetry images of heliostat mirrors at Sandia's NSTTF in different settings with UAV-integrated polarimetric imaging sensor. We are performing data analysis to estimate the optical error of heliostat mirrors based on polarimetric images.
2. We have developed simulation model for the polarization state of the ground; validated the model with outdoor measurements at ASU; aim to incorporate this model into flight planning for distinguishing heliostat facets from the background.
3. We have upgraded the gimbal-payload system upgrade to enable autonomous pointing and polarimetric imaging collection on the field.
4. We have improved the second generation polarimetric imaging drone system to improve the system stability.

5. We have collected polarimetry images of heliostat mirrors at Sandia's NSTTF in different settings with the second-generation UAV-integrated polarimetric imaging sensor. We performed data analysis to estimate the optical error of heliostat mirrors based on polarimetric images.

### *Concept and method*

Concentrated Solar Power (CSP) fields require valid and efficient methods to inspect the heliostats status. Among the issues that are commonly identified in the operation of the CSP field, optical error plays an important role that directly influences efficiency and safety. In recent years, the UAV-based scanning method for heliostat inspection has shown potential in achieving fast and non-intrusive inspection of the field. These methods mainly rely on the reflection image of certain objects into the target mirrors, where the difference between captured images and calculated images with optical model can be used to infer the optical errors of the heliostat and furthermore each facet. For example, the nonintrusive optical (NIO) method published in 2020 utilizes the reflection image of the tower in the CSP field [REF]. In the same year, another method named UFACET (Universal Field Assessment, Correction, and Enhancement Tool) was proposed and is still under development now. UFACET is an optical error inspection method based on and the HFACET (Heliostat Focusing and Canting Enhancement Technique). Instead of setting the camera at a fixed position like HFACET, UFACET uses an imaging drone to scan the field and determine the optical errors of multiple heliostats quickly with machine vision. However, both NIO and UFACET methods face contrast issues in certain scenarios using the conventional visible camera to detect the edge of the heliostats and mirror facets. As shown in Fig.7, during the scanning of the field using a UAV, there are several scenarios showing low contrast in a visible image. It is mostly due to the fact that the reflection of the mirrors shows similar intensity and contrast with its surroundings. While the edges and corners in these scenarios can be difficult to distinguish using a conventional visible camera, it is possible to introduce polarimetric imaging to help. Although the polarization information is not directly visible to human eyes, we can calculate and process different images using Stokes parameters, such as Degree of Linear Polarization (DoLP) image and Angle of Polarization (AoP) image. Fig.7b-c shows the simulations of DoLP and AoP while the Sun position is given. Utilizing the distinguishable pattern of the skylight polarization, it is possible to design certain angles of the camera to enable the polarimetric-aid contrast enhancement for heliostat inspection[5].

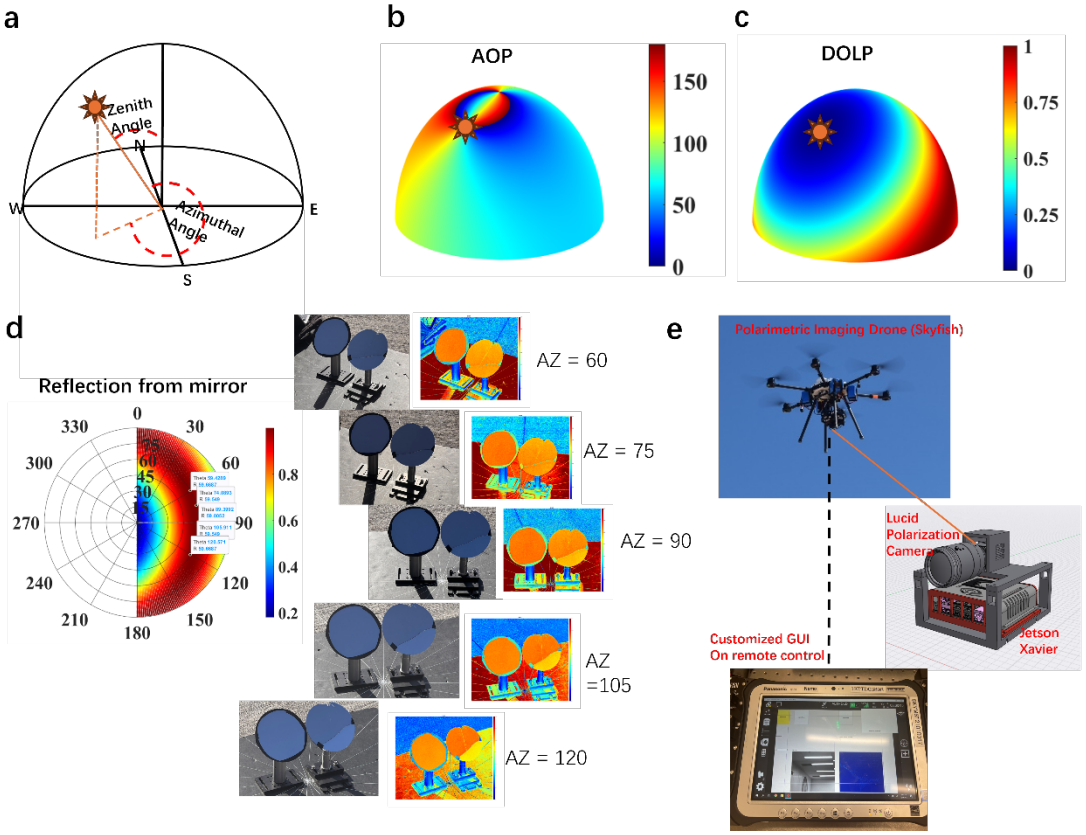


Figure 7. Polarized Sky Dome simulation based on Rayleigh scattering model and concept demonstration. **a**. Spherical coordinates definition. Azimuthal angle 0 starts from North and increases clockwise. Zenith angle 0 is pointing up to the sky zenith. **b,c** Angle of Polarization simulation with same Sun position to figure a. **d**. Demonstration of concept with small mirrors samples. The mirror on the right side has cracks. It can be seen from the images that the DoLP reflected by the mirror maintains high values as indicated on the reflection simulation. **e**. Polarization imaging drone setup used for field tests at Sandia National Laboratory.

Figure 7d demonstrates the results of small sample measurements we completed at ASU on April 17th, 2024. With the Rayleigh scattering simulation, we calculated the reflection DoLP from the mirror when they are facing away from the Sun and did azimuthal scan at 15 degrees step size from 60 to 120 degrees. The camera zenith was 60 degrees so that these angles fell into the region with the highest DoLP incidence. Scattering events in the air decreases the DoLP incidence and are subject to weather conditions. We can get relatively high DoLP up to around 0.7 on a sunny day with clear sky. Applying similar methods to heliostats, it is possible to find certain angles for the camera to acquire polarization images with high DoLP, different AoP, etc. To realize the in-situ inspection, we built a polarimetric imaging drone for fast scanning of the field, as shown in Fig 1e. We designed this polarimetric imaging drone with a Skyfish drone, Jetson Xavier as microcontroller and a Lucid Polarization Camera [REF each one to their site]. Our customized GUI allows the operator to view the live feed of the camera and capture images with the remote control. This system enables the field tests with the drone at Sandia NSTTF.

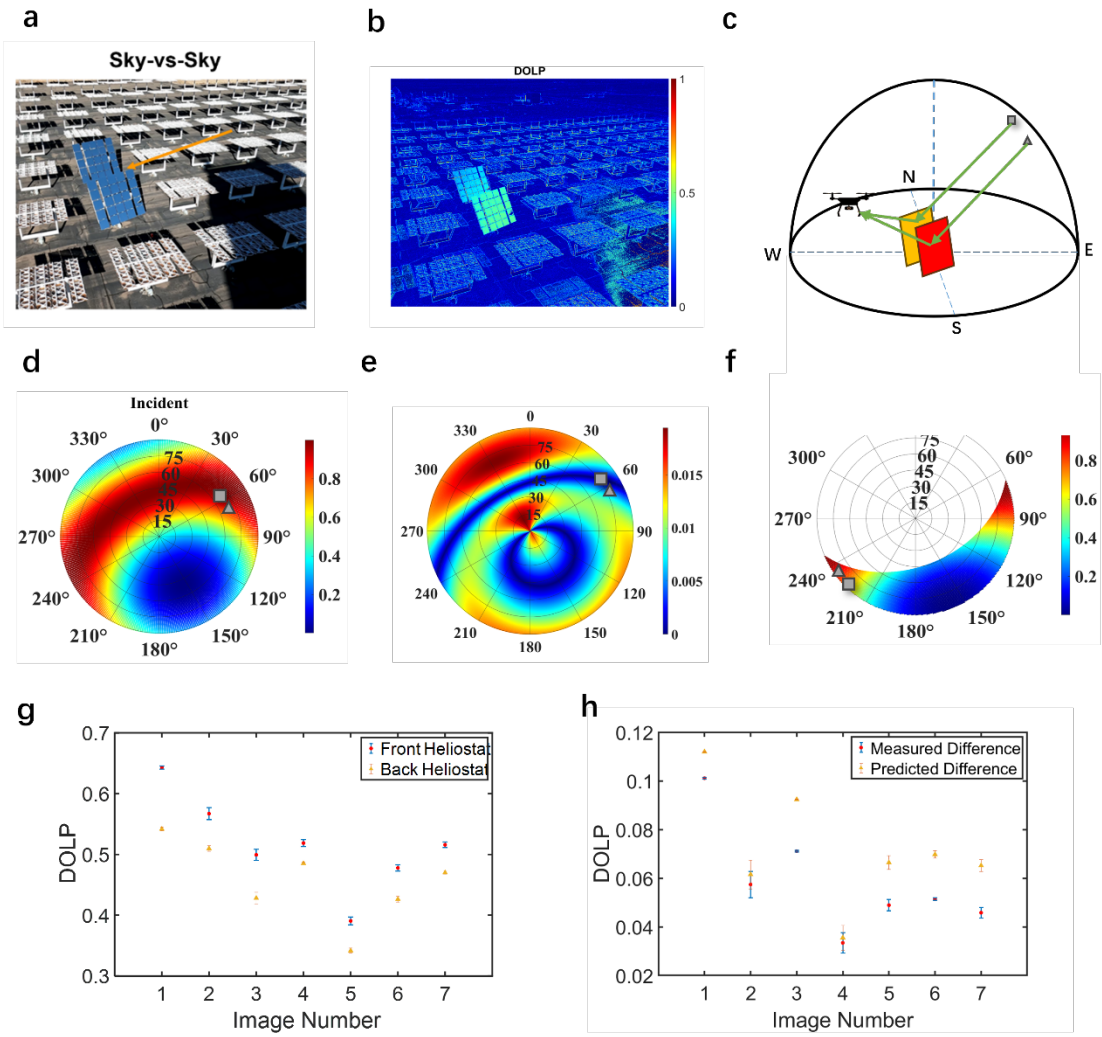


**Figure 8 Sky-v-sky scenario**. **a**. Image captured by visible camera showcasing sky-v-sky scenario. The overlapping edge is difficult to detect. **b.** Image captured by polarization camera showcasing sky-v-sky scenario. **c**. Schematics of reflection from adjacent heliostats results in different region of the sky, and thus different DoLP values. **d,e** DoLP and DoLP gradient simulations of these two heliostats' corresponding sky regions using the model presented in [5]. **f.** DoLP simulation of the reflection from these two heliostats. **g.** DoLP values comparison between front and back heliostats overlapping at the edge. **h.** The predicted DoLP difference between front and back heliostats and the measured difference acquired from the captured images. Image number indicating different images used for data.

When the field is in operation, all heliostats are focusing sunlight on the receiver, and thus adjacent heliostats point in a similar direction. When we take images with a drone camera, we often encounter a scenario where two adjacent heliostats overlap in the image, but only one of them is the target heliostat of interest. In the high-speed scanning method, the drone camera position is designed to look at the heliostats with their reflection towards the sky but without direct sunlight. In some situations, two overlapping heliostats both reflect blue sky, resulting in very similar intensity and color. This can result in a low edge contrast between them. As shown in Fig. 8a, the visible image can exhibit missing edges where overlap occurs. Such situations make fast and reliable detection of mirror edges and corners more difficult. With simulations shown in Fig. 8d-f, we can calculate the DoLP values and gradient of incidence, reflection from the mirrors, and

their difference. Since these adjacent heliostats are at different locations, their orientations are different as they are tracking the Sun and the collector on the central tower in a CSP field. With a small difference in their orientation angle in Fig. 8c, they can be reflecting the sky region with rapidly changing DoLP values and thus results in good contrast in DoLP image. Figure 8g and 8h show the results of 7 different polarization images captured during the field test. With the front and back heliostat having DoLP value with more than 0.05 difference respectively, the contrast can be enhanced for edge detection.

Overlapping heliostats image is not the only difficulty encountered during the inspection with a visible camera drone. When the drone is at a relatively higher elevation angle and is looking down on the heliostats, the reflection of the ground can get into the image. When the ground reflection is next to the real ground, as shown in Fig 9a, the contrast of the bottom edge is also significantly limited due to the similar color. With the AoP images, however, it is possible to get very different AoP values on the heliostat reflection and the ground. The heliostat mirrors are modeled mainly as a smooth and clean surface where the specular reflection can apply. Comparably, the ground has complicated surface morphology and the reflection from it cannot be seen as specular. To model such a rough surface, Torrance-Sparrow Model can be used as approximation. The rough ground surface is treated as a combination of numerous micro-facets while each of them reflects the incident light individually. The reflection result is a normalized integration of all the reflection rays from each micro-facet. The change of polarization during each reflection was calculated using Mueller Matrix derived from Fresnel Laws, as in equations (1-4). $S_R$ and $S_I$ denote the Stoke Parameters of reflected light and incident light, respectively. $M_{ab}$ is the reflection Mueller Matrix at interface of material a and b. $R_l$ and $R_r$ are the parallel and perpendicular reflection coefficients. $n_a$ and $n_b$ are the refractive indices of the two materials at the interface, while $\theta_a$ and $\theta_b$ are the incident and refractive angles.

$$S_R = M_{ab} \cdot S_I \qquad (1)$$

$$M_{ab} = \begin{pmatrix} \frac{1}{2}(R_l R_l^* + R_r R_r^*) & \frac{1}{2}(R_l R_l^* - R_r R_r^*) & 0 & 0 \\ \frac{1}{2}(R_l R_l^* - R_r R_r^*) & \frac{1}{2}(R_l R_l^* + R_r R_r^*) & 0 & 0 \\ 0 & 0 & \Re\{R_l R_r^*\} & \Im\{R_l R_r^*\} \\ 0 & 0 & -\Im\{R_l R_r^*\} & \Re\{R_l R_r^*\} \end{pmatrix} \qquad (2)$$

$$R_l = \frac{n_b \cos\theta_a - n_a \cos\theta_b}{n_b \cos\theta_a + n_a \cos\theta_b} \qquad (3)$$

$$R_r = \frac{n_a \cos\theta_a - n_b \cos\theta_b}{n_a \cos\theta_a + n_b \cos\theta_b} \qquad (4)$$

In the simulation shown in Fig.9c, the refractive index of the ground was set as 1.45 and 10,000 micro-facets were calculated. Fig. 9d is a result summary for 7 different images taken for the ground-v-ground scenario. In general, while the AoP difference between ground and heliostat is above 50 degrees, the contrast is significant statistically and visually.

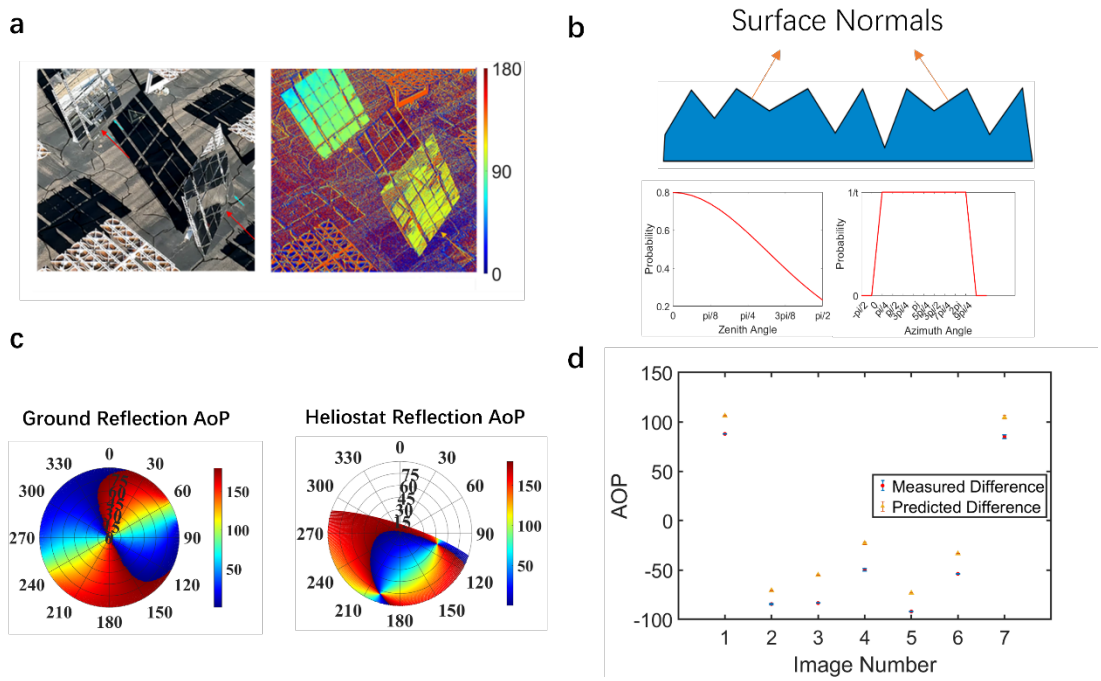


**Figure 9 Ground-v-ground scenario**. **a**. Images captured by visible camera and polarization camera (right) showcasing ground-v-ground scenario. **b**. Ground surface model based on Torrance-Sparrow model. It consists of numerous micro-facets and each facet's surface normal zenith angle follows a normal distribution while azimuthal angle follows a uniform distribution. **c**. Simulations of AOP reflected from the ground and from the heliostat. **d**. The predicted AoP difference between ground and heliostats and the measured difference acquired from the captured images. Image number indicates different images used for data.

### *Optical error determination*

Even though there are benefits of using polarization images, the requirement of the specific angles can be difficult to meet under all circumstances. In the field test, we capture polarization images as calculated by simulation, but also pick the ones with good contrast without limiting ourselves to a certain type of image. It is a flexible method and can benefit from image fusions of different polarization images as well as visible images. In Fig. 10a, the raw(intensity), DOLP and AOP images of the same capturing show that different edges can be found by different images. For example, the AOP image can be used to enhance the contrast of the bottom edge to ground, while DOLP images can be used to distinguish the reflection to sky. Fig.10b-d demonstrate the calculation process of optical errors adapted from UFACET. First the flight log's camera position is corrected using the corners of the target heliostat. Second, the ideal curvature was calculated using the design data of the heliostat 8E3. Third, using the captured images, the orientation error is corrected on 7E3. Eventually, each facet of 8E3 is used as a datapoint for calculating the azimuthal and zenith canting angles. These angles are compared with the ideal curvature to get the azimuthal error and elevational error shown in Fig.10e.

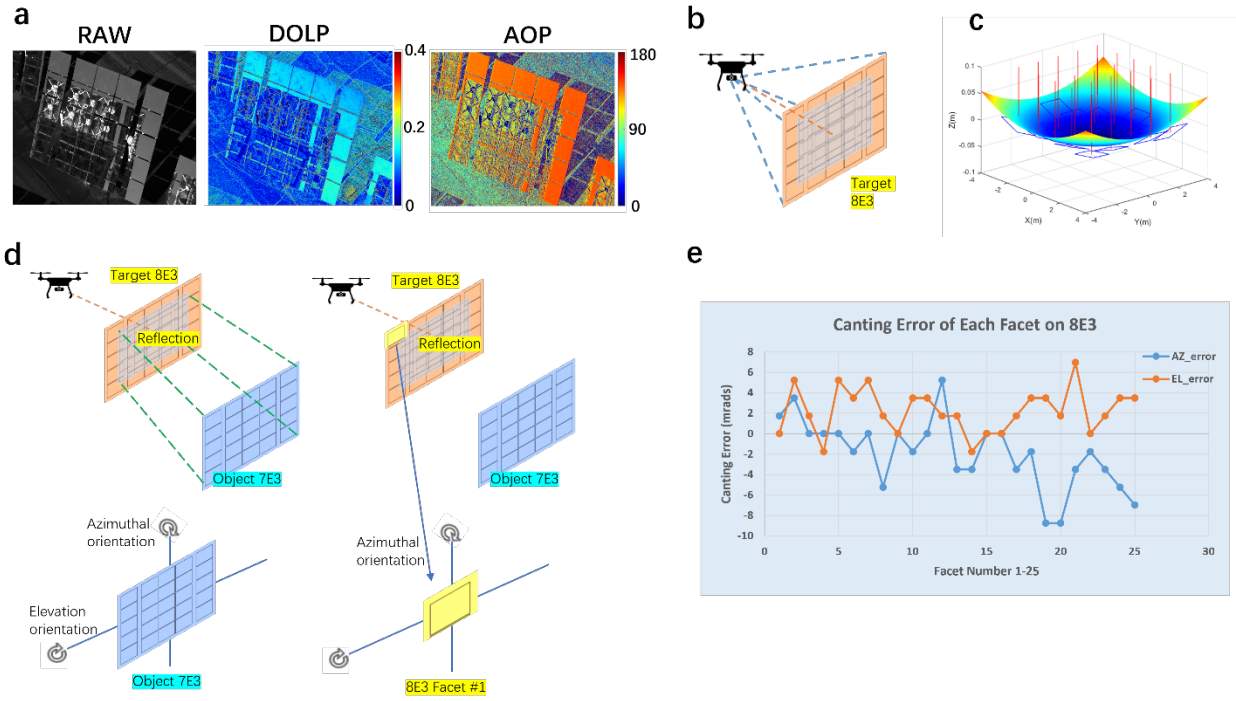


Fig. 10. **Optical error calculations based on captured images. a**, Raw, DOLP and AOP images of the heliostat 7E3 reflection in heliostat 8E3. **b**, Correction of the camera position and orientation using the heliostat corners. **c,** Ideal curvature calculation on 8E3 simulating the facets into a paraboloid surface. **d,** Similar to UFACET, the canting errors of each facet are calculated using the reflection image. **e,** Errors are calculated using result from the UFACET method and the ideal curvature of each facet.

Mirror cracks and scratches

During the field tests with the polarimetric imaging drone, we took images of heliostat mirrors with cracks. We have taken images both at a distance (> 20 m) and close (~10-15 m). Both can be used to identify the mirrors with cracks. The close-up image provides more details about the cracks due to higher spatial resolution (Fig. 9). Based on the measurement results, we concluded that high contrast detection of mirror cracks and scratches relies on 1) proper position of polarimetric imaging drone to achieve reasonably high DOLP (>0.4) of the mirror image and 2) at least 4 pixels for each 1 $cm^2$ on the mirror facets. (The crack width on the mirror is estimated to be ~1 mm. We could not measure the exact crack width.)
We took 198 images of heliostat mirrors with cracks in total at a distance of 10-15 meters and mirror image of sky portion with high DOLP (>0.2). A summary of the results

is shown in Table 1. A success rate of >90% has been achieved.

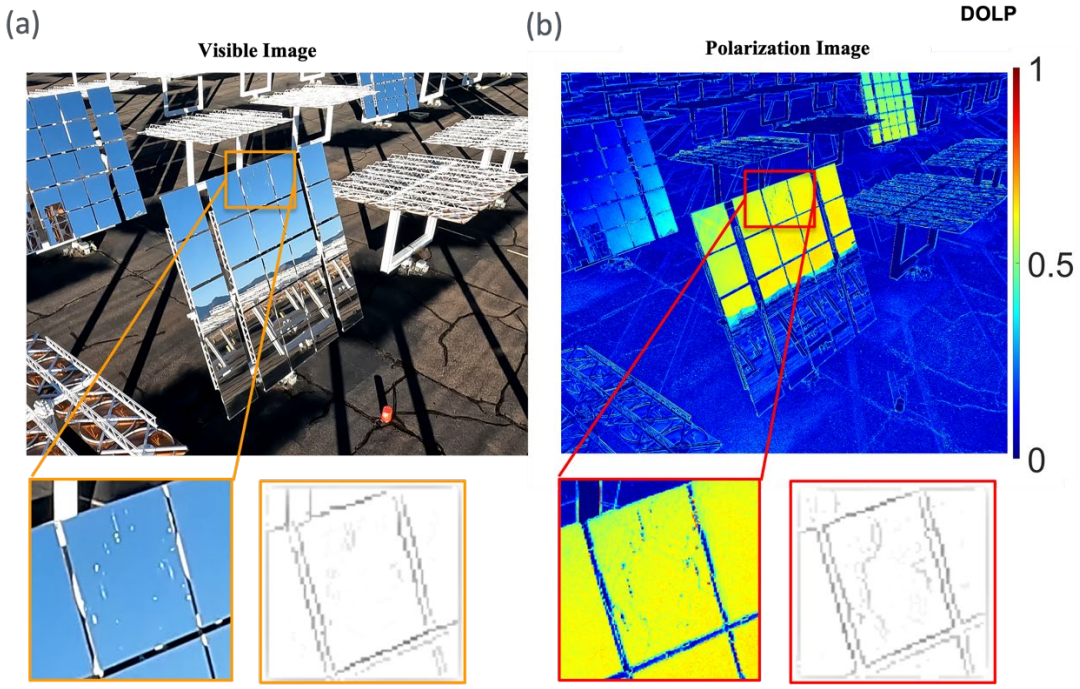


Figure 9 **Mirror defects detection.** (a) Visible images. (b) Polarimetric images taken close to the heliostat. Insets on the bottoms shows close-up view and the crack detection results.

Table 1: A summary of the field test results for mirror crack detection

| Time of the field test | **Successful** | **Unsuccessful** | **Total Images** | **Success Rate** |
|---|---|---|---|---|
| Dec2021 | 12 | 0 | 12 | 100% |
| Apr2022 | 168 | 12 | 180 | 93.33% |
| All | 186 | 12 | 198 | 93.94% |

## Task 3: Investigate the benefits and feasibility of applying polarimetric imaging to monitor mirror soiling condition

Technical progress and outcomes:

1. We have collected samples of soiled CSP mirrors and dust samples from the Sandia CSP test field (west of the solar tower) and characterized the size distribution of the dust particles at different regions on the mirror
2. We have developed theoretical models to simulate the polarization state of scattered light from mirrors with dust particles. We are yet to verify the algorithm by carefully checking the codes and comparing them with experiments with well-controlled parameters.
3. We performed the first field tests in CSP plants and collected satisfactory images for data analysis. We are working on analyzing the results.

### *Concept and modeling*

When light shines on the soiled mirror surface, it is partially reflected by the clean area and partially scattered by the soiled particles. To predict the reflectance using polarization images quantitively, we established the optical model to simulate the process of light scattering and reflection. The sunlight, after traveling through the atmosphere, forms the skylight that covers every direction of the sky dome because of Rayleigh scattering [17]. At different time, location and incident angle, the incidence light's polarization states can be calculated from Rayleigh scattering. When the incident light arrives at the mirror surfaces, it gets reflected by the clean part of the mirror and scattered by the soiled particles on the mirror. The scattering events caused the change of polarization states decreases the Degree of Linear Polarization. To get the best contrast, we put our camera in the position and orientation such that the reflected region of the sky from the mirror has relatively high Degree of Linear Polarization (DoLP) from the simulation of skylight. As time and location influence the sun position on the sky dome, this DoLP simulation pattern changes for each measurement, and the suitable camera positions shall be chosen differently according to each simulation. In this model, the soiled mirror can be seen as a mirror surface with multiple spherical particles in different sizes deposited on it. In Mie theory, the scattering coefficient is only dependent on the scattering cross-section and the refractive index of the particle. These particles are thus treated as spherical particles with the same refractive index as they are the same kind of soil. Statistically we are calculating the summation of the scattering events of each particle, thus the individual particle's shape and refractive index difference were neglected.

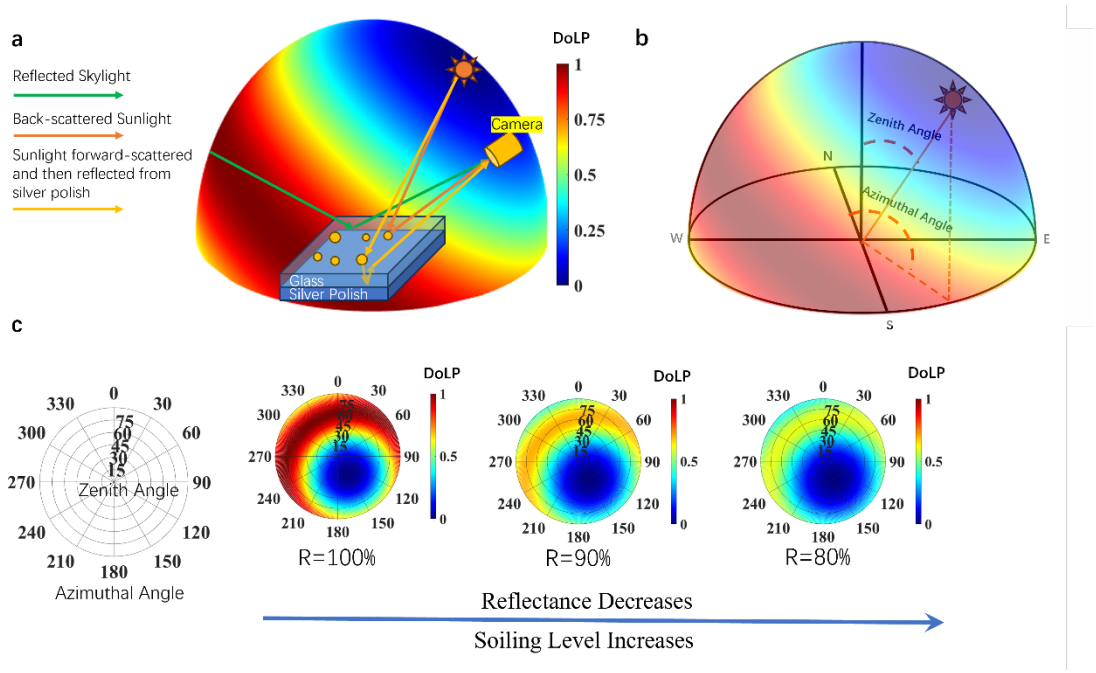


**Figure 10 Simulation Model to Predict Reflectance Using DoLP. a,** Diagram showing the considerations of light sources in the proposed model. The background is simulation of the skylight DoLP Pattern in 3D space as a dome. **b,** The spherical coordinates used in figure a, defined by azimuthal and zenith angle. **c,** Simulations showing that as soiling level increases, reflectance decreases. This simulation is a 2D projection onto the ground plane. The Azimuthal angle starts at 0 degrees at North and increases clockwise. Zenith angle starts at center and increases to 90 degrees at the boundary of the circular pattern.

We consider the light collected by the camera in two parts. First, for the area of the mirror that is not covered by any soiled particles, we consider it directly reflects the skylight of the corresponding angles, and the Stokes Parameters change during this reflection process can be calculated using Muller Matrix [18] as in equation (1-3). The specular reflection in percentage defined by this simulation model is the proportion of the clean area divided by the total area of the mirror surface. Here, $\mathrm{M_{ab}}$ denotes the Reflection Muller Matrix from medium a to medium b, $\mathrm{R_l}$ and $\mathrm{R_r}$ represent the parallel and perpendicular reflection coefficients of the Fresnel Equations at the interface between air and mirror, respectively.

$$\mathrm{M_{ab}} = \begin{pmatrix} \frac{1}{2}(\mathrm{R_l R_l^*} + \mathrm{R_r R_r^*}) & \frac{1}{2}(\mathrm{R_l R_l^*} - \mathrm{R_r R_r^*}) & 0 & 0 \\ \frac{1}{2}(\mathrm{R_l R_l^*} - \mathrm{R_r R_r^*}) & \frac{1}{2}(\mathrm{R_l R_l^*} + \mathrm{R_r R_r^*}) & 0 & 0 \\ 0 & 0 & \Re\{\mathrm{R_l R_r^*}\} & \Im\{\mathrm{R_l R_r^*}\} \\ 0 & 0 & -\Im\{\mathrm{R_l R_r^*}\} & \Re\{\mathrm{R_l R_r^*}\} \end{pmatrix} \quad (1)$$

$$R_l = \frac{n_b \cos\theta_a - n_a \cos\theta_b}{n_b \cos\theta_a + n_a \cos\theta_b} \qquad (2)$$

$$R_r = \frac{n_a \cos\theta_a - n_b \cos\theta_b}{n_a \cos\theta_a + n_b \cos\theta_b} \qquad (3)$$

Second, for the area of the mirror that is covered by the soiled particles, the scattered sunlight is dominant as the sunlight intensity is way higher than skylight [19]. The scattering of skylight is not considered in this model. The simulation results of adding these skylight scattering components were demonstrated and there was no significant difference. For the scattering of sunlight, some of the sunlight will be back scattered into the viewing angle of the camera and thus is collected into the sensor; some will be forward scattered and reach the back of the silver coating, and then get reflected. This process only considers one scattering event and is calculated using the Mie Scattering theory [20]. The sum of these two sources of collected light forms the image and we can then model the Degree of Linear Polarization as a function of soiling level as expressed in equation (4).

$$S_{total} = (S_{sun})_{scat} A_P K_{sun} + (S_{sky})_{refl} A_{NP} K_{sky} \qquad (4)$$

$S_{total}$ is the total Stokes Parameter. $(S_{sun})_{scat}$ is the Sunlight's Stokes Parameter after scattering off the soiled particle and $(S_{sky})_{refl}$ is the Skylight's Stokes Parameter after reflection off the clean mirror. $A_P$ and $A_{NP}$ denote the Area Percentage of the sample covered by soil particles and not covered by soil particles, respectively. $K_{sun}$ and $K_{sky}$ denote the Sunlight and Skylight intensity ratio. By definition, we have the relation as following.

$$A_P + A_{NP} = 1, \qquad K_{sun} + K_{sky} = 1 \qquad (5)$$

With the calculated Stokes Parameters collected by the camera, we can then determine the relationship between Reflectance and DoLP. According to the simulation, higher soiled particles coverage leads to lower clean area, and thus lower reflectance as well as DoLP. In Fig.10c, this relationship was shown with a simulation of flat mirror reflection at different soiling coverages assumptions. However, in this equation, the ratio of sunlight and skylight, which varies according to the weather conditions [19], is unknown. When changing this ratio, the simulation curve describes the change of DoLP according to reflectance is changed. Therefore, in the measurements, we first do a reference sample

measurement to determine this ratio by fitting the curve with the reference sample data points, and then proceed to measure the test samples or heliostat mirrors.

***Outdoor measurements***

To validate this model before carrying out a field test, several measurements with small mirror samples were taken at the top floor of Arizona State University's parking garage to avoid building blocking skylight. These measurements were set up in a similar manner. We prepare multiple samples using the same type of sand for each measurement. These samples are round silver mirrors with different soiling levels in the three soiled regions and one clean region. Based on the simulation of skylight DoLP pattern at different time and location, the angle ranges were selected to have the relatively high DoLP after reflecting from a soiled mirror. Next, the polarization camera (Allied Vision Mako G-508B POL) set on a tripod was placed to the desired azimuthal and zenith angle. After adjusting the focus of the lens and locating the mirror to the center of the image frame, the raw image was captured and later processed to be a DoLP image. Among various images taken at different angles during the scanning process, we select the image with the highest DoLP values in the clean region to get the data points for the DoLP in each region.

On the same day as the measurement, the reflectance of each mirror region is also measured with an optical setup. As shown in Fig.11, after the data was acquired, we fit the simulation curve's sunlight and skylight ratio parameters with the reference sample's DoLP and reflectance of the four regions. With the fitted curve, we input the DoLP values of each region on other samples and predict their reflectance. These Samples Under Test (SUT) were created in the same way as the reference sample with the same type of sand. Next, the predicted reflectance and the measured reflectance are compared to get the model prediction error to represent the accuracy. Fig.11e shows the predicted reflectance mapping of the mirror after fitting the model. In this case, the lowest data point on the mirror still has more than 90% reflectance. For different mirror and soiling types, the lowest reflectance on the mirror could be different, and the corresponding mapping should have dynamic range based on the lowest value. In total, we have prepared and measured four different types of sand following the same procedures described above. Even though the fitting results are different for different types of sand and different date of measurement, the error between the predicted reflectance using DoLP image and fitted model and the measured reflectance is always lower than 3%, as shown in Fig.11h.

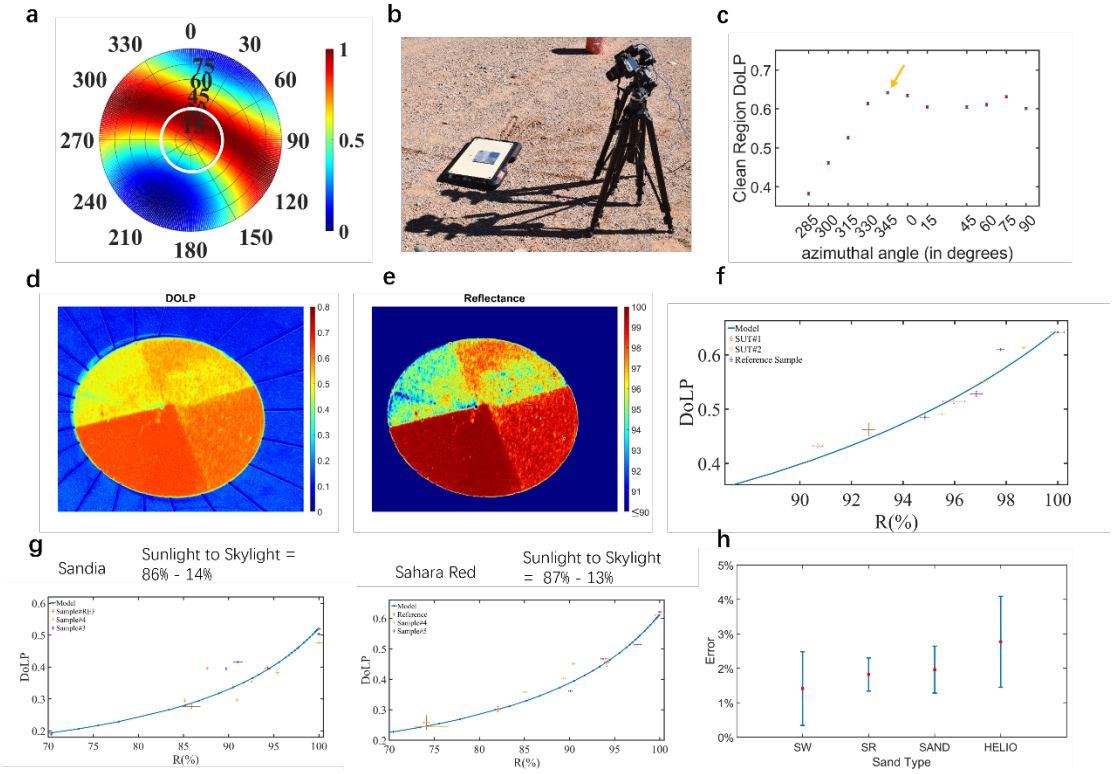


**Figre 11 Small Mirror Sample Measurement. a,** DoLP simulation of reflection off the mirror placed on ground. The camera was set at 30 degrees zenith and scanned from 285 degrees azimuth clockwise to 90 degrees azimuth. **b,** Experiment setup with polarization camera fixed on a tripod. The mirror sample was placed on a black cardboard to reduce the scattering of the environment. **c,** Median values (red dots) and standard deviation (blue error bars) of the clean region DoLP measured at different azimuthal angle. The highest DoLP median was 0.6418 at 345 degrees azimuthal angle. **d,** Selected image at 345 azimuthal angle the clean region has the highest DoLP. Each region's DoLP values were taken at a one-inch area and the values written on the image are the median value of the selected area. **e,** The relative reflectance mapping of corresponding regions after fitting the data with DoLP and reflectance measurement of sampling points in the four regions of the mirror. **f,** Fitting curve of the four data points from the reference sample and the error of the two Sample Under Test (SUT). The sunlight to skylight ratio was acquired at 86% to 14%. Error was defined as the difference between the predicted reflectance from the fitted curve and the measured reflectance of the SUTs. Overall, the error was always under 3%. **g,h,** Measurement results for four different types of sand tested at ASU. The x-axis label corresponds to "Sahara White (SW)", "Sahara Red (SR)", "Sandia Sand (SAND)", "Sandia Heliostat Samples (HELIO)". Average errors of these four measurements were 1.41%, 1.82%, 1.96%, 2.77%.

### *Field Deployment with Integrated System*

So far, we have developed and validated the polarization-based reflectance prediction method. When it comes to field deployment, factors such as heliostats tracking, safety concerns, flight path or measurement positions, deployable systems need to be considered thoroughly. We designed two systems to accommodate different scenarios of field inspections. For CSP fields that require quick, large area soiling detection, we

designed an integrated polarimetric imaging drone system [15] to execute precalculated waypoints and capture images of multiple target heliostats in one flight. For CSP fields that require detailed soiling detection on individual mirror facets, or limit the use of drones, we designed a portable setup that can be manually carried or installed on a ground vehicle to capture the polarization images. Two field tests at Sandia National Solar Thermal Test Facility (NSTTF) in Albuquerque, New Mexico were carried out respectively using each setup on July 14$^{th}$, 2023, and Oct 20$^{th}$, 2023. On July 14$^{th}$, we captured images of heliostats with different soiling levels with the UAV-based setup. These images were captured while the test heliostats were at their Beam Characterization System (BCS) tracking position [21] to set the conditions such that the detection was carried out non-intrusive to the operation of the field. Since the tracking point and sun position of different time can be pre-calculated, simulation was done beforehand to find the position and direction of the camera. As shown in Fig.12a, because now the heliostats mirrors are at a certain angle respective to the ground, the simulation of reflection also changes accordingly. We flew the polarimetric imaging drone to the pre-calculated waypoints and adjusted camera orientations to capture the images with high DoLP values. The heliostats had the center facet cleaned up the day before the field test to provide the baseline of relative reflectance. After the flight tests were done, we used reflectometer (Surface Optics 410-Solar Solar Reflectometer) to measure multiple points on each target facet to get the reflectance information. The DoLP region was selected to be consistent with the reflection measurements. Then, by applying to the model, we calculated the fitted curve of reflectance to DoLP, as shown in Fig.12f. Because different mirror facets of the heliostats correspond to a different region of reflection, we adapted correction method for the DoLP and R values in the model fitting. First, the measurements with reflectometer 410-Solar that has an error range over 10% are neglected. These errors are introduced by manually holding the device to the facet surface. The DoLP results captured, and the Reflectance measured are then used to fit the model and calculate the error. Over different measurements, we find our accuracy of different points are in a range of 0.5% to 8% after fitting adjustments.

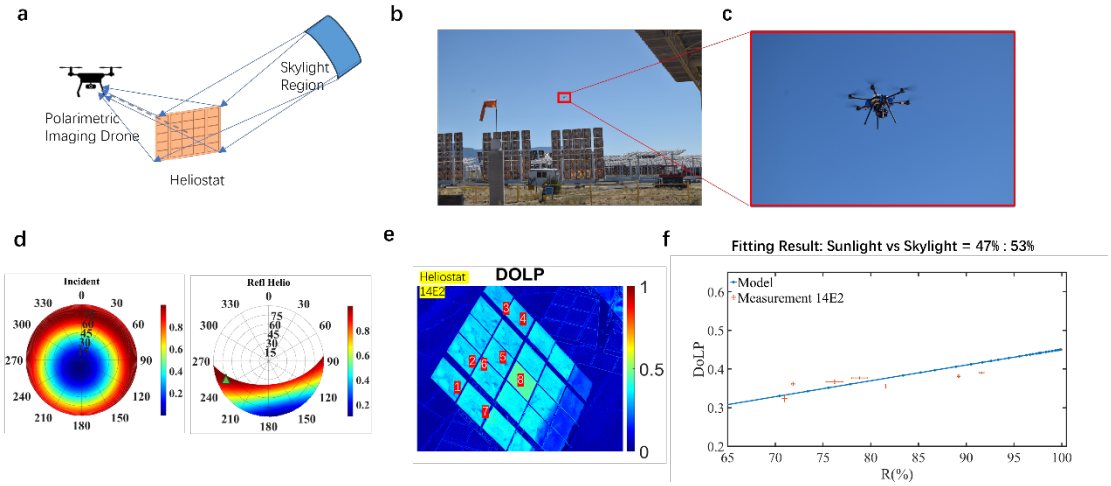


**Figure.12 Flight Test Setup and Results. a,** Flight Test diagram. The polarization camera was integrated on a UAV and takes images of the heliostat from designed positions to look at the reflection of desired skylight regions. **b,c,** Field Test Images. The image in the red box shows the polarimetric imaging drone. **d,** Incident Skylight Simulation and Heliostat Reflection Simulation for the Flight Test. Since the drone needs to fly higher than the heliostat during the tracking status, angles larger than 90 degrees zenith are neglected. The green triangle indicates approximately the position where the image in (e) was taken. **e,** DoLP Image Of 14E2 Taken During the Flight Test. This image was taken at 13:35 on July 14th, 2023 while the heliostat 14E2 was tracking for BCS standby at 13:30. The red numbers indicate the approximate positions where the reflectance measurements were taken and thus the datapoints used in fitting. **f,** Fitting Results of the Flight Test. As shown in (**e**), 8 data points were used in total while number 8 was in the "clean" region. This region was cleaned by the field crew before the test. The error bars were acquired using the standard deviation of Reflectance(horizontal) and DoLP(vertical). The heliostat was commanded to face directly South. The portable system was lower than the heliostat bottom row of mirrors and thus used zenith angle at 105 degrees, as indicated by the green triangle in (**d**).

On Oct 20th, 2023, another field test was carried out using portable setup. The goal of this test was to provide an alternative method for fields with other limitations that cannot use an imaging drone. With the portable setup, it enables the operators to use zenith angles larger than 90 degrees, or below the horizon. It is still possible to do autonomous detection if the setup is embedded with GPS module and an autonomous vehicle on the ground. In our case, we ordered the heliostats to stop tracking and directly facing south for personnel to enter the field safely at Sandia NSTTF. A reference sample was first measured following the procedures to get the fitted curve. Then, we captured several images of different facets on the bottom row of the two target heliostats to get the DoLP values. The reflectance was measured beforehand using the 410-Solar reflectometer and it was easier to find the corresponding regions of interest. Fig.13d shows the measurement and fitting results, and the error ranges from 0.5% to 6%.

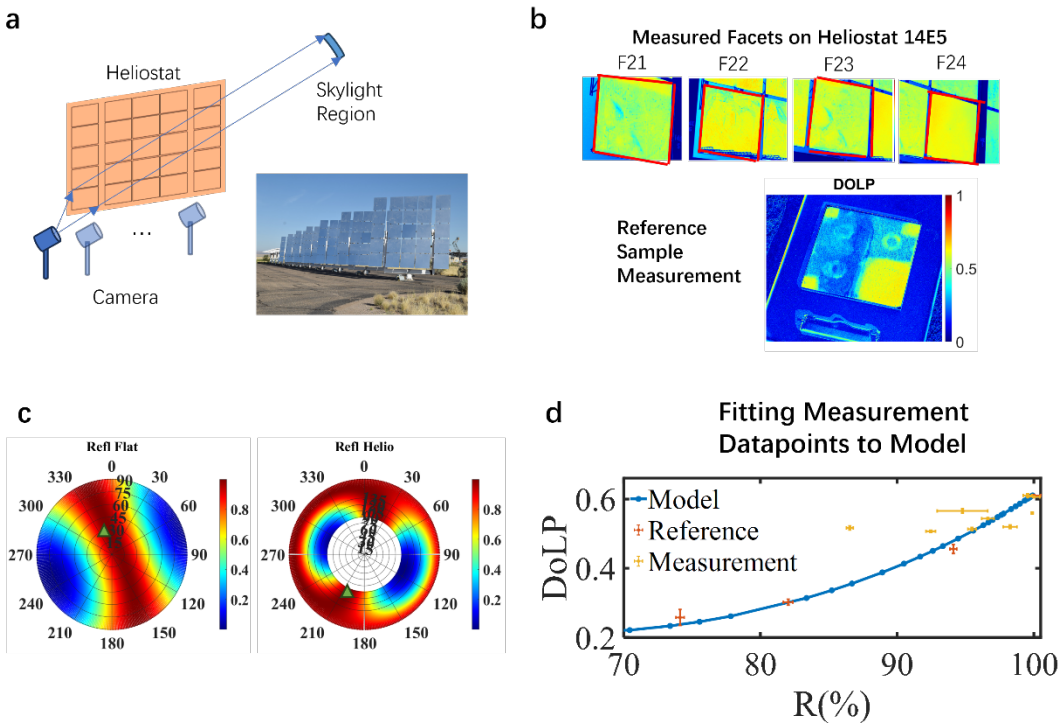


**Figure 13 Portable Setup and Field Test Results. a,** Measurement Diagram with a Portable Polarimetric Imaging System. The camera is close to the heliostat compared to the flight test. Thus, five images were taken as the camera moved parallel to the heliostat. **b,** DoLP Images Captured with Portable System. F21 to F25 indicate the facet number of the heliostat 14E5 bottom row. Reference sample was measured while lying flat on the ground. The red lines mark the boundary of each mirror of interest. **c,** Skylight Simulation Reflected by the Flat Reference Sample and Heliostat Reflection Simulation for the Portable System Test. **d,** Results of the Measurement Compared with the Fitted Curve Using the Reference Sample. Datapoints with larger than 10% in error bar were neglected.

## Task 4: Investigate the feasibility of applying polarimetric imaging to monitor CSP receiver tubes

Technical progress and outcomes:

1. We have collected samples of soiled CSP mirrors and dust samples from the Sandia CSP test field (west of the solar tower) and characterized the size distribution of the dust particles at different regions on the mirror
2. We have developed theoretical models to simulate the polarization state of scattered light from mirrors with dust particles. We are yet to verify the algorithm by carefully checking the codes and comparing them with experiments with well-controlled parameters.

***Collect information about receiver tube defects and the needs of CSP plants regarding receiver tube inspection***

The objective of this task is to determine if it is feasible to apply polarimetric imaging techniques to monitor CSP receivers for risks of damage, actual damage before any catastrophic events with the receiver like tube rupture.
The Sandia team collected images of receiver panels with both conventional imaging sensor and the ASU polarimetry imaging system. These receiver panels (from Solar 1 and 2 receivers) are on display at NSTTF; therefore, these receiver panels are not operational (i.e., cannot be heated up), but they do exhibit varying levels of paint (or coating) degradations. The goal is to 1) explore possible types of defects on receiver panels and 2) check the feasibility of enhancing receiver defects with polarized images.

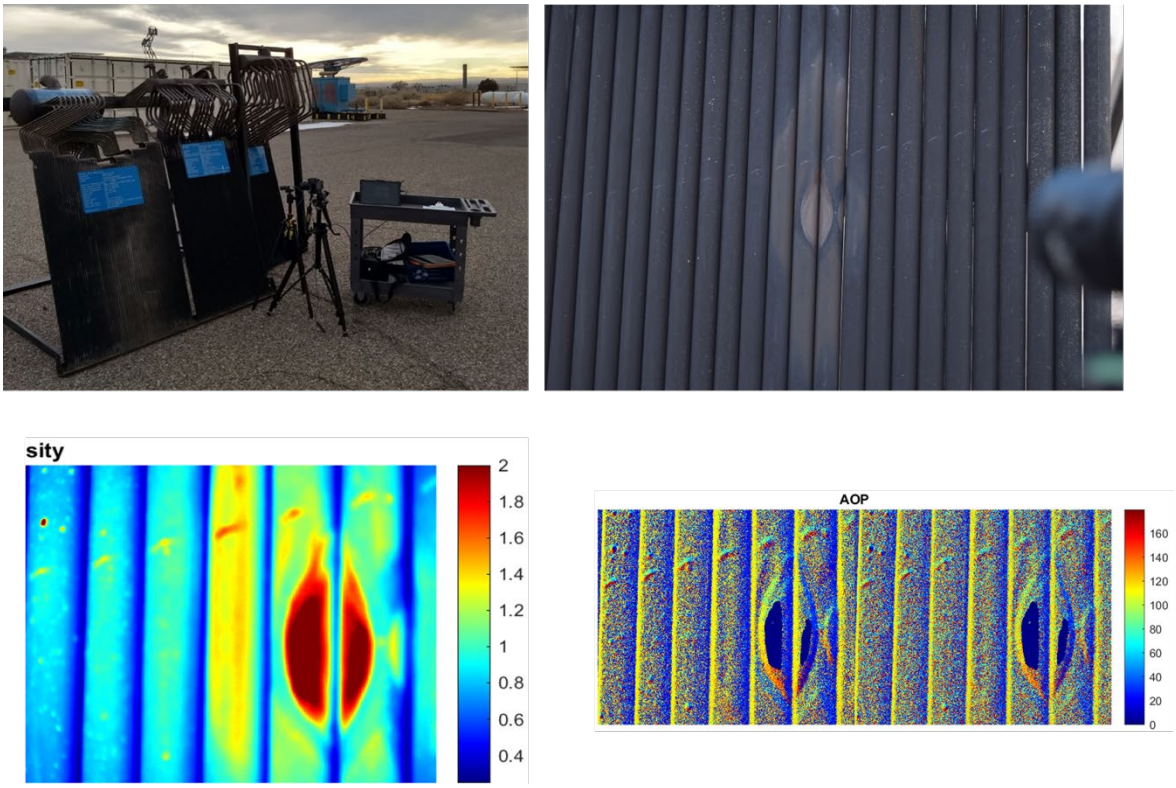


Figure 15: (a) Receiver image setup. (b) Example Nikon image.
(c) Polarimetry image (0°). (d) Angle Of Polarization (0°).

The polarimetry images for a portion of the receiver clearly show defects such as scratches and areas with missing black paints with much higher contrast than conventional photo images.

***Investigate the feasibility for applying visible/ infrared polarimetric imaging to monitor receiver tube defects***

The objective of this task is to determine if it is feasible to apply polarimetric imaging techniques to monitor CSP receivers for risks of damage, actual damage before any catastrophic events with the receiver like tube rupture. Updates on this subtask include

discussions with the team (including Sandia) on how to collect some representative receiver tube samples.

Previously, we have collected images of receiver panels at Sandia with both conventional imaging sensors and the ASU polarimetry imaging system. The polarimetry images for a portion of the receiver clearly show defects such as scratches and areas with missing black paints with much higher contrast than conventional photo images. We performed theoretical analysis for the polarization states of scattered light from receiver tubes. In this model, we consider receiver tubes with 2-inch diameter tubes and nanoscale and microscale particles on the surface. We can perform the calculation to obtain the polarization state of scattered light for different input polarization states, including linear polarization, circular polarization, partial polarization and unpolarized light.

Figure 15a shows the coordinate setting for the model. Figure 15b-15d show the simulation results of polarization images of an array of receiver tubes. Our simulation results show that for different input polarization states, different incident angles, the periodic features in the AOP image all exist originated from the Mie scatter of particles on the receiver tube. Figure 15e and 15f show the measurement results obtained as described in the previous paragraph. The AOP images obtained by simulation and measurement agree reasonably well. Compared to visible images of these black tubes, the polarimetric images show very clear features reflecting the surface morphology. The results we obtained so far suggest it is promising to use visible polarimetric imaging to detect receiver tube defects, such as scratches, deformation, and regions of missing paints. Compared with visible imaging technology, polarimetry imaging could provide much better contrast to enable early detection of defects, esp. cracks, scratches, instead of leaving them to get worse over time and eventually cause major failures. We are making CSP receivers and plan to use them to conductor more outdoor tests to optimize the detection method and evaluate the detection accuracy.

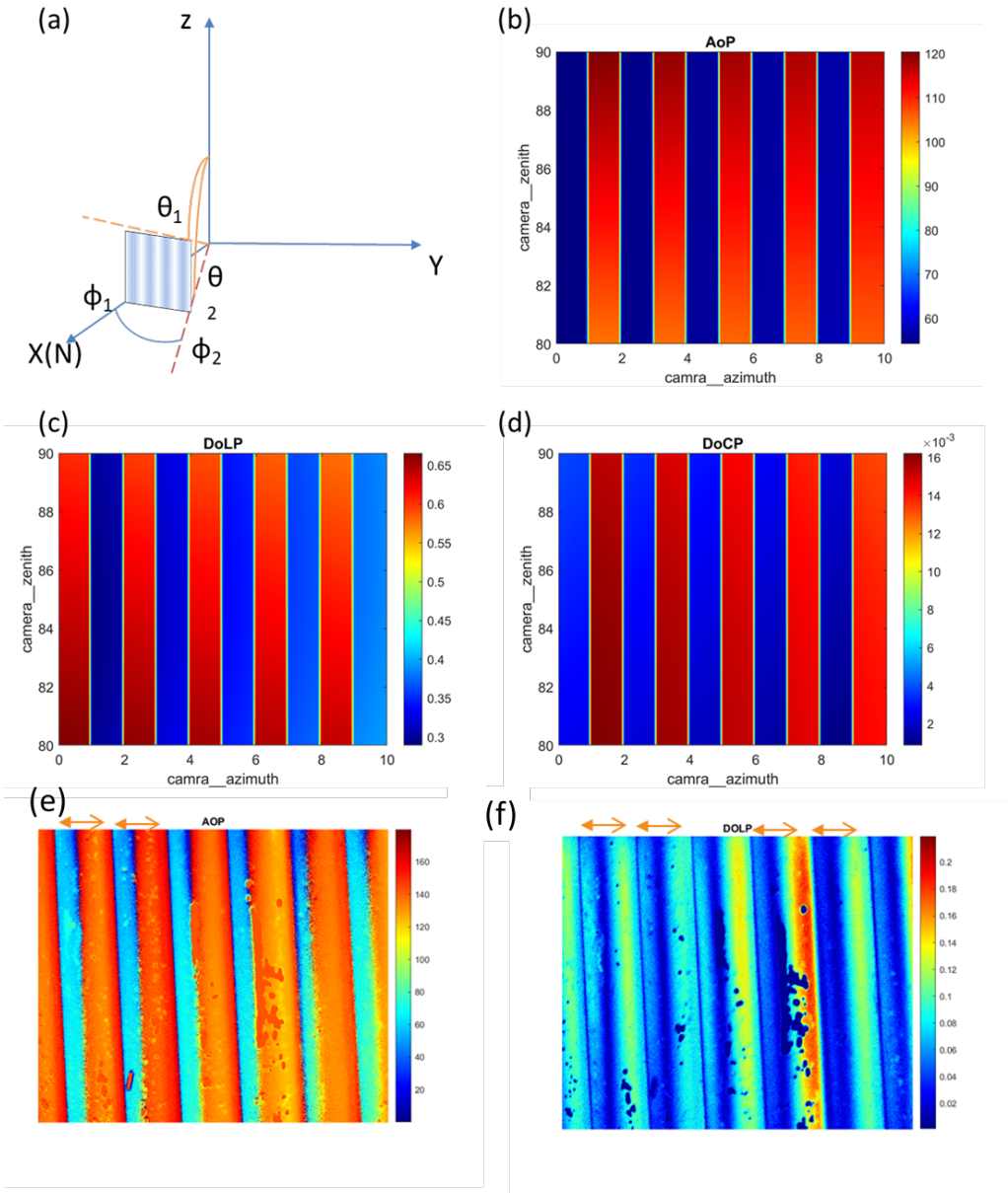


Figure 16 Simulation and measurement results of polarimetric images for CSP receiver tubes. (a) coordinate setup for the simulation (b)(c)(d) simulation results for polarization images. AOP: angle of polarization; DOLP: degree of linear polarization; DOCP: degree of circular polarization.

## Task 5: Perform techno-economic analysis and develop a commercialization plan

We have performed literature studies and some preliminary measurements to understand the potential applications of the full-stokes polarimetric imaging systems. We have identified four applications (besides CSP plant inspection) where full-stokes polarimetric imaging is preferred over conventional imaging and linear polarization imaging. Based on the information collected, we performed the value proposition of on-chip full-stokes polarimetric imaging sensors and drone-integrated polarimetric imaging sensors compared to state-of-art technologies.

### *Modeling Analysis*

The stated objective of the milestone is to detail sources of increased energy efficiency >5% and O&M cost reduction opportunities >10%. Economic and total power generation will be simulated using NREL System Advisor Model, in which the team has significant experience in both trough and tower techno-economic studies. In order to make estimates of LCOE/Yearly Power Output (MWh), we will be examining the sensitivity of several drivers in the Heliostat Field inputs, which tie to the proposed benefits of the project. Unfortunately, SAM does not allow detailed analysis of dry-brush cleaning protocols for the field.

Each of these items requires a model that correlates the expected improvement in the parameter to the expected benefits that aerial inspection can provide. For example, we know that in a normal range of analysis, a 1% increase in mirror reflectance decreases LCOE by approximately 1%. Cleaning the mirror can increase the reflectance to 95-96%, which is the factory specification. Therefore a trade-off needs to be made between the maintenance costs of cleaning (deionized water, labor, fuel) and the energy efficiency benefits. Therefore each driver (or input to SAM) is broken down into assumptions or data points which are used to calculate its value. Some items are not repeated but drive multiple inputs (EG labor costs).

- Canting error (mrad)
  - Outcome: Improve efficiency by correcting canting errors
  - Detectable errors by drone
  - Actionable error justifying intervention (driven by financial analysis)
  - Labor Rate
  - Hours to make the intervention
  - Material Cost to Make Intervention
- Mirror Reflectance and Soiling (%)
  - Outcome: Improve efficiency by improving cleaning protocol
  - Detectable soiling level or reflectance
  - Actionable error justifying intervention (driven by financial analysis)
  - Variance across the field of the above metrics
  - Hours to make the intervention
  - Material Cost to Make Intervention
- Heliostat Availability (uptime %)
  - Outcome: Improve Heliostat Availability by detecting defects early
  - Detectable cracks or defect parameters (minimum size detectable)
  - Costs defrayed via early intervention (repair vs. replacement)
- Water Usage per wash ($L/m^2$)
  - Similar to Soiling analysis
- Washes Per year (count/year)
  - Similar to Soiling analysis

### *Techno-Economic Analysis (TEA)*

The objective of the Techno-Economic Analysis is to discover if the additional cost of aerial inspection of CSP heliostats creates economic value. This is done by comparing the cost to inspect the field (device total cost of ownership + operator wages) plus the cost to perform corrective action (materials + labor) versus the potential increased revenue from energy sales.

*Image Error Detection and Correction TEA*

As discussed previously, a heliostat's optical errors can have a variety of sources. Surface slope error, heliostat shape errors, and tracking errors all contribute to total overall optical error as defined by

$$\sigma_{tot} = \sqrt{\sigma_{sp}^2 + 4\sigma_{surf}^2 + 4\sigma_{sh}^2 + \sigma_{tr}^2} \quad (1)$$

where $\sigma_{tot}$ is total optical error, $\sigma_{sp}$ is specularity error, $\sigma_{surf}$ is surface error, $\sigma_{sh}$ is shape error, and $\sigma_{tr}$ is tracking error. There is an angle doubling effect for errors resulting from surface orientation.[19] For the purposes of this analysis, specularity error is assumed to be zero per typical manufacturing standards in the mirror industry. Furthermore, the sun's intensity distribution (sunshape) is not considered in this analysis. The default value for single axis total error ($\sigma_{1ax}$) in NREL System Advisor Model's Molten Salt Tower CSP model is 1.53 mrad, which reflects Sunshot program goals. SAM assumes the orthogonal errors are identical, so the calculated conical total error is thus

$$\sigma_{tot} = \sqrt{2 \cdot 4\sigma_{1ax}^2}. \quad (2)$$

Increasing the total image error results in lower total energy production for a facility due to spillage losses. While spillage can be mitigated through larger receiver design, a complex relationship exists between allowable heliostat optical error and a receiver's size, costs, and radiative losses.

The UFACET project seeks to achieve canting errors of .25 to .50 mrad following detection and correction. For the purpose of analysis, we assume a "factory" 0.25 RMS mrad canting error which degrades quickly due to events and/or slowly due to degradation. The total Slope Error thus increases according the formula from Andraka and Yellowhair[14] :

$$SE' = \sqrt{SE_0^2 - CE_0^2 + CE'^2} \quad (3)$$

Rearranged, we can estimate the canting error present when varying the slope error input to NREL SAM.

$$CE' = \sqrt{SE'^2 - SE_0^2 + CE_0^2} \quad (4)$$

This technique assumes a baseline level of slope error coming from tracking, surface nonuniformities, and other sources, but allows us to examine the economic impact of canting error which we can detect and correct.

Using SAM's Parametric analysis tool, the Net Energy to Grid (kWh/year) and Total Electricity Revenues ($/year) metrics were tracked while varying Image Error from 0 mrad to 10 mrad. Figure 17 illustrates the relationships between image error, estimated canting error, and Power Purchase Agreement revenues which are assumed to have a simple contract at $100 per MWh. Due to limitations in SAM, there is no ability to specify heliostat sectors as having different image errors or imputed canting errors.

The revenue analysis thus assumes the entire heliostat field has uniform canting error for the entire year. This is not realistic, but, in combination with the total facet count, it does

allow us to create a “lost value” function for each month that a given facet has defined canting error. In the simulation run for Fig. 18, there are assumed to be 8790 heliostats with 16 facets each (4 facets x 4 facets, 12.2 m x 12.2 m, 97% reflective area to profile). For the sake of example, if we assume a given facet has a 5 mrad canting error, then the lost revenue in a month of misalignment is calculated as follows:

$$Lost\ Revenue\ \left[\frac{\$}{facet \cdot month}\right] = \frac{R(CE_0)[\frac{\$}{year}] - R(CE)[\frac{\$}{year}]}{12\ [\frac{months}{year}] \cdot 8790[heliostats] \cdot 16[\frac{facets}{heliostat}]}$$

$$= \frac{\$57{,}178{,}300 - \$46{,}736{,}006}{12 \cdot 8790 \cdot 16} = \$6.19$$

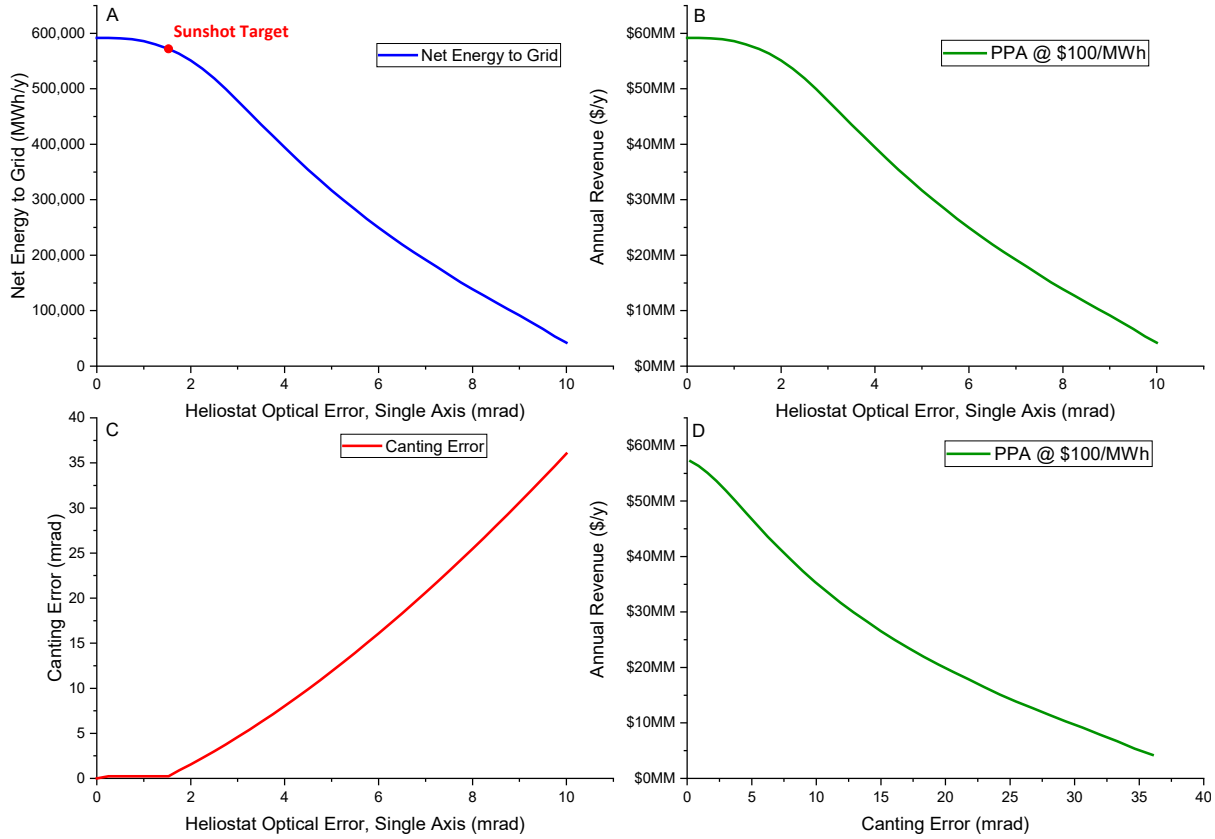


**Figure 18.** NREL SAM Simulation of Molten Salt Tower using default values; (A) Net Energy to Grid while varying Heliostat Properties:Image Error [slope, single-axis] (mrad); (B) Total Annual Revenue from Net Electricity Sales while varying Image Error (mrad); (C) Estimated Canting Error contributing to Slope Error per Equation 4; (D) Total Annual Revenue from imputed Canting Error while varying Image Error in NREL SAM.

Clearly, this oversimplifies the impact of heliostat distance to tower, temporal variations in irradiance, and other operational factors, but it does give us a starting point for estimating the value of canting misalignment detection. In order to estimate the value of an aerial inspection service, we need to make some assumptions about how the facets become misaligned. After all, if every facet in the field stays perfectly aligned for its entire

service life, then there is no value in inspection. At present, the author was unable to find data detailing the "accumulation" of facet image errors in test or operating power tower fields. This should be a priority for the research effort to demonstrate the potential value of the technology. The challenge will be that each heliostat design will have its own profile of failures over time, and current CSP efforts are primarily bespoke installations with quality metrics highly dependent on local contractors' efforts. The following table shows the primary assumptions used in the economic model:

| Drone Assumptions | | | |
|---|---|---|---|
| Drone - Price | $ | 25,000 | |
| Drone - Payload Price | $ | 2,000 | |
| Drone - Operator Wage + Benefits | $ | 37.74 | $/hr |
| Drone - Power Consumption while Operating | | 0.60 | kW |
| Drone - Working Life | | 5.00 | Years |
| Drone - Yearly Maintenance Costs | | 25% | |
| Drone - Purchase Price of Electricity | $ | 0.07 | $/kWh |
| Drone - Inspection Time Per Heliostat | | 1.00 | minute |
| Drone - Hours of Daylight to Inspect | | 8.00 | hours |
| Drone - Desired Period to Inspect all Heliostats | | 7.00 | days |
| Drone - Operator Hours Per Drone per Day | | 1.00 | hours/drone-day |

| Image Error Study | | | |
|---|---|---|---|
| Electricity PPA Price | $ | 0.10 | $/kWh |
| Electricity PPA Price | $ | 100 | $/MWh |
| Heliostats in SAM Simulation | | 8,790 | |
| Facets (X) | | 4 | |
| Facets (Y) | | 4 | |
| Facets per Heliostat | | 16 | |
| Intial Canting Error | | 0.25 | mrad |
| Canting Error Accumulation per Year | | 0.50 | mrad |
| $(\text{Probability of Event in a Week})^{-1}$ | | 1000 | |
| Probability of Event in a Week | | 0.001000 | |
| Canting Error Resultant from Event | | 10.00 | mrad |
| Fixed Correction Schedule Period | | 52.00 | weeks |
| Inspection Threshold Misalignment | | 0.80 | mrad |
| Labor Hours Per Correction | | 0.50 | hours |
| Maintenance Wage + Benefits | | 37.74 | $/hour |
| Materials Cost Per Correction | $ | - | |

**Table 2. Primary Economic Assumptions, Image Error Study**

In order to estimate the value of the inspection technology, we examine three maintenance strategies and two modes for accumulating canting error:

Maintenance Strategies:

1. No Image Error Detection or Correction : Simply, the errors in the field are allowed to accumulate over time. The lost revenue is calculated weekly according to the method described previously.

2. Scheduled Maintenance : The facet is realigned to factory specification on a set schedule. The length of the maintenance period was optimized using techniques discussed later. The costs are the sum of calculated maintenance labor costs and lost electricity costs from image errors. A very short maintenance period overweights the maintenance costs relative to the lost electricity costs, while the opposite is true for a very large period. The optimal period (a decision parameter) depends greatly on many assumptions including labor costs, probability of failure, and the shape of the lost electricity curve (Fig. 18D).
3. Detect and Correct : This assumes the aerial inspection technology works as desired. When the canting error detected by the aerial inspection process exceeds an assumed value, we assume corrective action is taken within a week, restoring the facet to its factory canting specification. In this case, the decision parameter to optimize is the acceptable canting error threshold. Again, “overmaintenance” as experienced by a very low canting error threshold results in a similar tradeoff described above.

Error Accumulation:

We examine a single facet over the course of 10 years using 52 week analysis units in a Microsoft Excel Spreadsheet. Both gradual and event-driven canting errors occur and are additive until maintenance.

1. Linear Degradation: the canting error is assumed to increase by a fixed increment each week. This models the gradual accumulation of errors due to mechanical stresses and fixture deformation. This has been witnessed in older heliostat fields, but the author was unable to quantify this effect.
2. Stochastic: the canting error is assumed to occur randomly with a defined increase in canting error in the case of an event triggering. Therefore the two important assumptions are the probability of an event occurring in a week for a given facet and the increase in canting error resulting from the event. This has qualitatively been noted to occur during the dry-brush and deluge cleaning processes. This effect is extremely important for this analysis, as the rigorous inspection process facilitated by aerial inspection is “overkill” if the only failure mode was a highly predictable degradation over time.

One can understand the combinations of failure accumulation and maintenance strategies by examining Figure . This chart is for illustrative purposes, and demonstrates two instances of the thousands of simulations which were run. In Fig. 19A, no stochastic events occur. The canting error grows linearly over time unless corrected according to a 52 week schedule (Scheduled and Corrected) or when it reaches a measured value of 1.5 mrad (Inspected and Corrected). Figure 19B is compares the strategies when two stochastic events occur in weeks 178 and 254. The “No Maintenance” strategy allows tremendous error to accumulate in the facet. The Scheduled Maintenance plan allows the error to stay high until the next maintenance period, so the economic severity will depend on how close the random event occurs to the planned maintenance event. The Detect and Correct strategy will detect the misalignment and repair it immediately. The weekly lost revenue due to grows with canting error severity as implied by Fig 19.

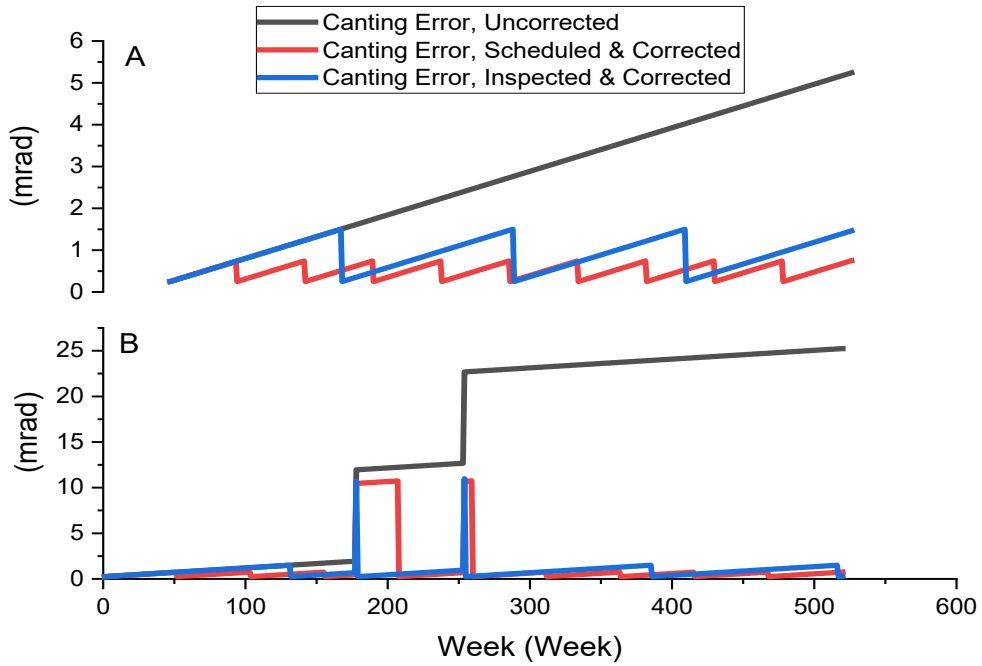


**Figure 19** Comparison of Maintenance Strategies in two different scenarios for illustrative purposes.: A) A stochastic event does not occur. B) A stochastic event occurs in week 178 and week 254.

To reiterate, this economic analysis is performed on a single facet, as simulating the weekly performance of the assumed ~140,000 facets over a long period was beyond the scope of the analysis. We acknowledge there could be correlations to stochastic events occurring on adjacent facets on a given heliostat, but these are not examined as there is no field data confirming or disconfirming this hypothesis. Conversely, there could be efficiencies from aligning all facets on a given heliostat if one is known to be far out of a alignment, but this is also beyond the scope of this preliminary analysis.
The figure of merit to minimize is total cost per facet per year, which is defined as:

$$Total\ Cost\ Over\ 10\ Years\ \left[\frac{\$}{facet}\right] = ME \cdot MEC + LR + IC \quad (5)$$

Where:
ME = Maintenance Events [events/facet]
MEC = Cost per Maintenance Event [$/event]
LR = Lost Revenue [$/facet]
IC = Inspection Cost [$/facet]

The inspection cost using some basic assumptions turns out to be quite small and immaterial to our analysis (). If we assume an operator can let the drone be autonomous and allocates only 1 hour per drone per day, the total costs end up being close to $0.01 per facet per week.

| **Cost of Image Error Inspection** | | | |
|---|---|---|---|
| *Drone Inspection Calculations* | | | |
| Heliostats Per day | | 480 | heliostats/day |
| Desired Time to Inspect all Heliostats | | 7.0 | days |
| Heliostats in Field | | 8790 | heliostats |
| **Drones Required (Round Up)** | | **3** | **Drones** |
| **Operating Drone-Hours Per day** | | **24** | **Drone-Hours** |
| | | | |
| *Drone Amortization & Maintenance* | | | |
| Cost of Drone & Payload | $ | 27,000 | $/drone |
| Life of Drone & Payload | | 5.00 | years |
| Yearly Depreciation Drone | $ | 5,400 | $/year |
| Yearly Maintenance Cost per Drone | $ | 6,751 | $/year |
| **Total Yearly Depreciation & Maintenance** | **$** | **36,454** | **$/year** |
| | | | |
| *Electricity Expenses* | | | |
| Drone - Power Consumption while Operating | | 0.60 | kW |
| Total Electricity Consumed Per Day | | 14.35 | kWh |
| **Yearly Electricity Cost** | **$** | **367** | **$/year** |
| | | | |
| *Labor Expenses* | | | |
| Drone - Operator Hours Per Drone per Day | | 1.00 | hours/drone-day |
| Total Operator Hours Per Year | | 1095 | hours |
| Labor Rate, incl. Benefits | $ | 37.74 | $/hour |
| **Total Labor Expenses** | **$** | **41,329** | **$/year** |
| | | | |
| ***Total Expenses Per Year*** | **$** | **78,150** | **$/year** |
| ***Total Expenses Per Facet Per Week*** | **$** | **0.01** | **$/facet-week** |

**Table 3. Costs of Drone Inspection**

Using Oracle Crystal Ball Monte Carlo software, we ran 10,000 simulations for 30 different values for the Canting Error Threshold (mrad) decision parameter. The value we derive for this optimal threshold is highly dependent on all assumptions used for the economic model. The shape of the chart indicates the threshold for intervention is between 0.75 and 1.0 mrad.

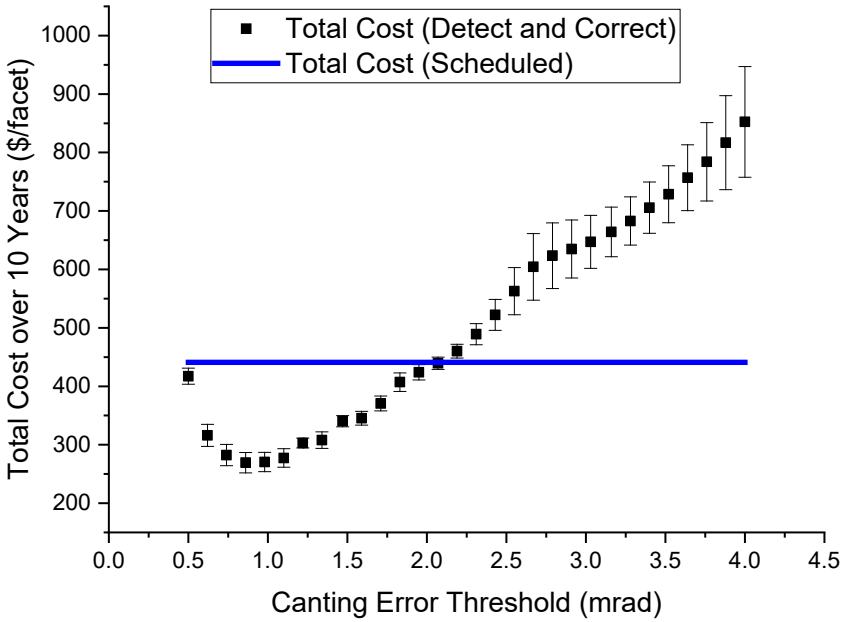


**Figure 20. Optimization of the Canting Error Threshold:** Total Cost per facet over 10 years as defined by Equation 5**.** The optimal threshold of ~.85 reduces net lost electricity costs per facet over 10 years by from $440 to $270. Error bar is the standard deviation.

Including all costs of drone inspection and maintenance events, the potential value created versus the "business as usual" scheduled maintenance plan is the difference between the total cost of detect and correct at the optimal value and the total cost of scheduled maintenance. Again these values are highly dependent on the assumptions of the model, but the estimated value creation from aerial detection of errors is $440 - $270 = $170 per facet over 10 years.

**For the reference plan in NREL SAM's Molten Power Tower model with 8790 heliostats (12.2 m X 12.2 m) and 16 facets per heliostats, this results in a savings from preventing spillage of $2.4 million per year. Using the same system for soiling detection, we expect revenue increase by up to 5%, i.e., $3 million per year. The reality is that this number, though, is incredibly dependent on the gradual degradation assumption (mrad/year), the stochastic misalignment event probability, and the misalignment magnitude pending a stochastic misalignment.**

**Subtask 5.3: Reach out to potential industry partners to find out their interests in full-stokes polarimetric imaging sensors as well as drone-integrated polarimetric imaging systems**

Our research progress has attracted interests from researchers and industry on biomedical imaging, polarization microscope and chip inspection. We are discussing potential collaborations with them.

***Application in polarization microscopy and muller matrix microscopy***

In conventional optical microscopes, image contrast of objects mainly results from the differences in light intensity and/or color. Muller matrix optical microscopes (MMMs), on the other hand, can provide significantly enhanced image contrast and rich information about objects by analyzing their interactions with polarized light. However, state-of-art MMMs are fundamentally limited by bulky and slow polarization state generators and analyzers. Here, we demonstrated the feasibility of applying metasurfaces to enable a fast and compact MMM, i.e., Meta-MMM. We developed a dual-color MMM, in both reflection and transmission modes, based on a chip-integrated high-speed (>20fps) metasurface polarization state analyzer (Meta-PSA) and realized high measurement accuracy for Muller matrix (MM) imaging[6]. The Meta-PSA can simultaneously perform full-Stokes polarimetric detection for thousands of spatial points (readily scalable up to millions of points) in a single snapshot. We demonstrated the Meta-MMM in both transmission and reflection modes with high measurement accuracy for full-Stokes polarimetric imaging and MM imaging (MM measurement errors are about 1% to 2% ) for red and green colors. Compared with the state-of-art MMM systems, our proposed Meta-MMM is featured with ultra-compact, high speed (~2 s per MM image, limited by the CMOS imaging sensor), compact and simple system configuration. Furthermore, we applied the proposed Meta-MMM system to characterize nanostructured thin films, silver dendritic particles, and also discovered for the first time the optical birefringence in honeybee wings, suggesting its broad applications in material and structure characterization, industrial inspection, biological study, etc

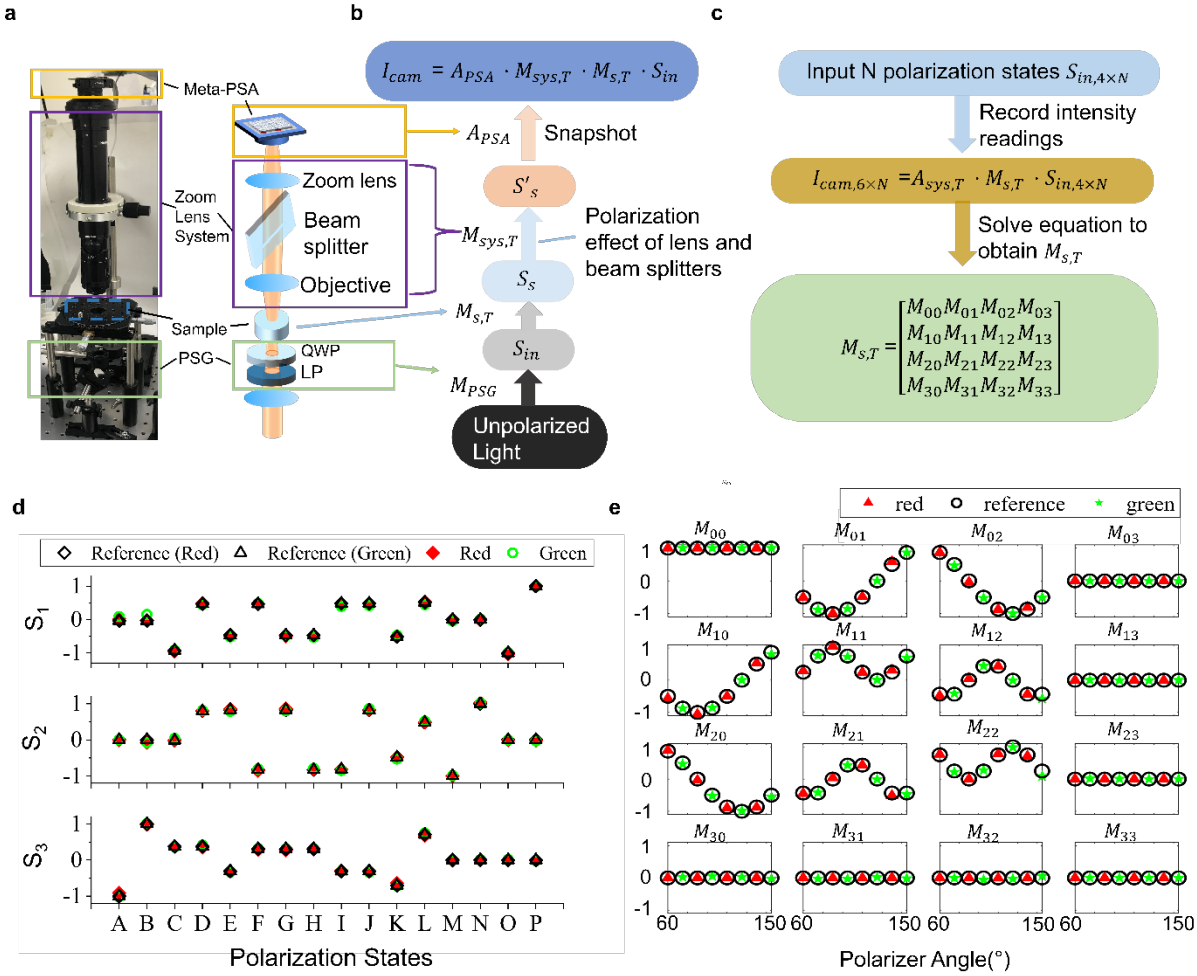


**Figure 21: Full Stokes polarization detection of polarization states and Mueller matrix measurement.** **a**, Photograph of meta-MMM showing Zoom lens system as objective, polarization state generator (PSG) in transmission mode, lens sets, and Meta-PSA. The corresponding field of view (FOV) and microscopic imaging resolution are 1.16mm×0.82mm, 3.66μm at the lowest magnification (×1.16) and 96 μm×67.9 μm, 0.83 μm at the highest magnification (×28), respectively. **b**, Flowchart for Stokes parameter measurement using Meta-MMM (transmission mode) based on the Instrument matrix method. **c**, Flowchart for MM measurement using Meta-MMM (transmission mode) based on the Instrument matrix method. **d**, Transmission mode full Stokes parameter measurement error of 16 arbitrary polarization states under 630 to 670nm (red square) and 480 to 520nm (green circle) input, respectively. Black hollowed square: theoretical values of Stokes parameters as a reference, red color; Black hollowed triangle: theoretical values of Stokes parameters as a reference, green color; red square: Measured results of Stokes parameter for red color; Green hollowed circle: Measured results of Stokes parameter for green color. **e**, Transmission mode MM measurement of a standard linear polarizer at different polarization axis angles. Black hollowed circle: theoretical values of a linear polarizer as reference. Red triangle: measured MM component results with red color input (630 to 670nm); green star: measured MM component results with green color input (480 to 520nm). Figure adapted with permission from reference [6]

## *Characterization of thin film structures*

Muller matrix measurement has been widely used to characterize thin film structures, unveiling their birefringence, depolarization, scattering, and chiral properties. Here, we apply Meta-MMM to characterize an optical metasurface (OM) thin film structure with artificial birefringence designed for polarization control [2]. Studying the linear and circular retardance or diattenuation properties of optically thin artificial metamaterials[7] can facilitate the development of novel flat optical devices with high performance and low cost for numerous applications, such as metalens and plasmonic metasurfaces for polarization detection and polarimetric imaging [8-11], etc. The microscopic and SEM images of Si metasurface composed of subwavelength Si nanogratings are shown in Fig. 22a. The Si metasurface exhibit strong optical linear birefringence and can function as a linear retarder [2] with the fast optical axis along U axis and slow axis along V axis (Fig. 22b). For incident light linearly polarized along *x*-axis, the transmitted light is converted into RCP at wavelengths around 500 nm (green light) and LCP at wavelength around 630 nm (red light). This is because the phase difference $\Delta\varphi$ between U (fast) and V (slow) axis are $\frac{3}{2}\pi$ at 500 nm and $\frac{1}{2}\pi$ at 630 nm (Fig. 22c). We used our meta-MMM to obtain the MM images of the Si metasurface and extracted the linear retardance from MM images (Fig. 22d) using Lu-chapman MM decomposition method[12]. The spatially averaged linear retardance of Si metasurface on the left side (Figure 22d) are 0.436 π in red) and -0.557π in green, respectively, which agrees well with simulation results. In addition, we compared measurement results of polarization conversion obtained by Meta-MMM with results taken by a traditional PSA using rotating linear polarizer and quarter waveplate to evaluate measurement accuracy. The degree of circular polarization (DOCP) images of light after passing the Si metasurface taken by Meta-MMM using 0° LP as input is shown in Fig. 22e. We obtained the spatially averaged value of DOCP image (spatial resolution:1.45μm) (left in Fig. 22e), i.e., -0.872 for red color and 0.813 for green, respectively. We also measured the DOCP of light transmitted through the Si metasurface using the traditional PSA as shown in Fig.22f. The averaged converted DOCP values at red and green colors are -0.885 and 0.805, respectively. Thus, the extracted measurement error for DOCP is less than 2%. Such high accuracy single-shot polarimetric imaging and high speed MM imaging of nanostructured thin film structures confirms the great potential for applications of Meta-MMM in material science and nanophotonic research.

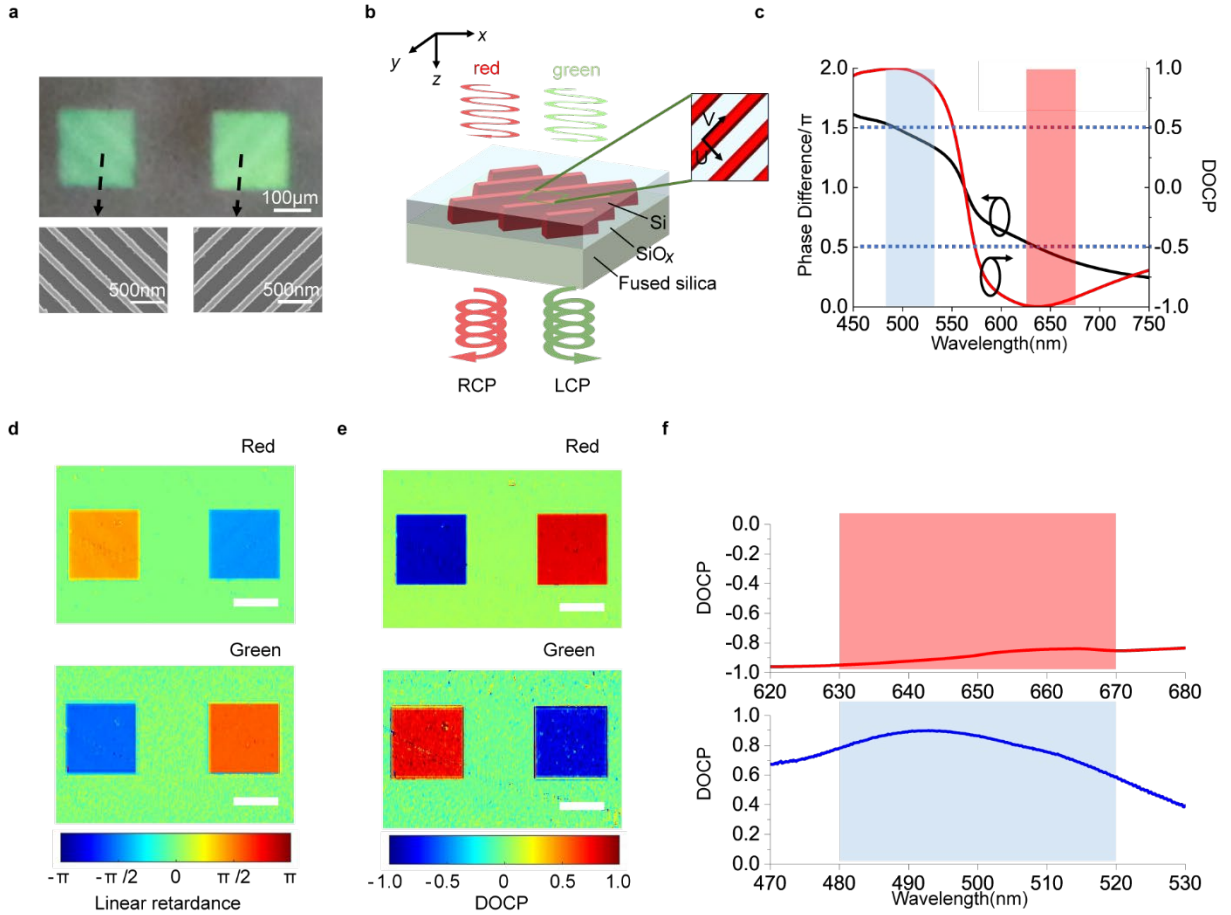


**Figure 22 : Characterization of optical birefringence in Si metasurface thin film structures**
**a**, Optical microscope (top) and scanning electron microscope (SEM) (bottom) images of the fabricated Si metasurface structures. **b**, A 3D schematic of the Si metasurface. The width, period, and thickness of Si nanogratings are ~100nm, 297nm, and 130nm, respectively. **c**, Left axis: Simulated phase difference between fast (U) and slow(V) axes. Right axis: converted DOCP for LP input polarized along the *x*-axis. **d**, Linear retardance image of Si metasurface for red and green color input, respectively. Scale bar: 100μm. Image Magnification: ×10. **e**, DOCP image measured by polarization microscopy under red and green color input, respectively. Scale bar: 100μm. **f**, The DOCP of transmitted light measured by PSA using the traditional method at red and green color respectively. Figure adapted with permission from reference [6]

### *Characterization of complex metallic structures: silver dendrites*

Polarization and Muller matrix images are also useful for characterizing and analyzing materials with different surface morphology and scattering properties. In this work, we applied Meta-MMM to inspect the material properties of silver dendrites. Dendritic silver nanoparticles (AgNPs) are a type of dendrite-shaped conjugated metallic particles that can be fabricated via electrochemical[13], photochemical[14] methods, etc. The porous and metallic material property of these silver dendrites allow them to be optically scattering and absorptive, making them suitable for chemical sensing[15] and chemical catalysis[16]. In addition, the growth process of silver dendrites follows random Brownian motion; thus, the fractal shape of formed silver dendrites is always unique and this, couples with their nanostructure, makes them intrinsically unclonable and therefore ideal for physical tags for anti-counterfeiting applications[14, 17]. Despite a tremendous

amount of effort in the chemistry and nanofabrication of silver dendrites, studies on the polarization effect introduced by unique material properties of silver dendrites are still at an early stage and of great interest, as polarization properties of silver dendrites induced by optical scattering can potentially reveal its surface morphology. Figure 23a shows a zoomed-in image (×2) of silver dendrite grown by the electrochemical method [18]. The conjugated silver dendrites are typically a few μm thick and consist of silver nanoparticles that are ~ 30 to 50 nm in diameter, as shown in Fig. 23b. A lot of empty space exists between the silver nanoparticles, leading to a highly porous structure. As a comparison, we fabricated a thin film structure made of silver with the same patterns but a smooth surface using UV lithography, silver deposition, and lift-off processes, as illustrated in Fig. 23c. Figure 23d shows a zoomed-in image (×2) of the fake sample. The fabricated silver structures have a continuous and smooth surface profile with grain size at the scale of ~30-50 nm, as shown in the SEM image in Fig. 23e. We took polarization and MM images using the Meta-MMM in reflection mode with red light illumination. Figure. 23f shows the intensity and DOCP images for the authentic silver dendrites (top) and Fig.23g shows the fake ones (bottom) under RCP light illumination. The intensity images of the two samples are quite similar. Yet, their DOCP images are easily distinguished because the silver dendrites have a strong depolarization nature due to their porous surface morphology, while the silver thin films in the fake sample have optically smooth surfaces and thus reflect light without reducing the DOCP. The depolarization images of both samples (Fig. 23h) were obtained by taking MM images and performing MM decomposition using the Lu-chapman MM decomposition method[12]. The depolarization of silver dendrites is indeed very high due to materials scattering and absorption, while the depolarization of the fake sample is close to 0. This study suggests the potential application of polarimetric imaging for dendrites characterization and detection to authenticate the true (electrochemical) patterns and avoid sophisticated copying/counterfeiting, as the fractal shape can possibly be duplicated via image algorithms (as we did for the fake sample), whilst the duplication of unique surface morphology of the silver dendrites is much harder. Similarly, such surface morphology analysis can also be applied for other applications such as industry inspection[19], solar thermal energy[20] and, catalyst [21], etc.

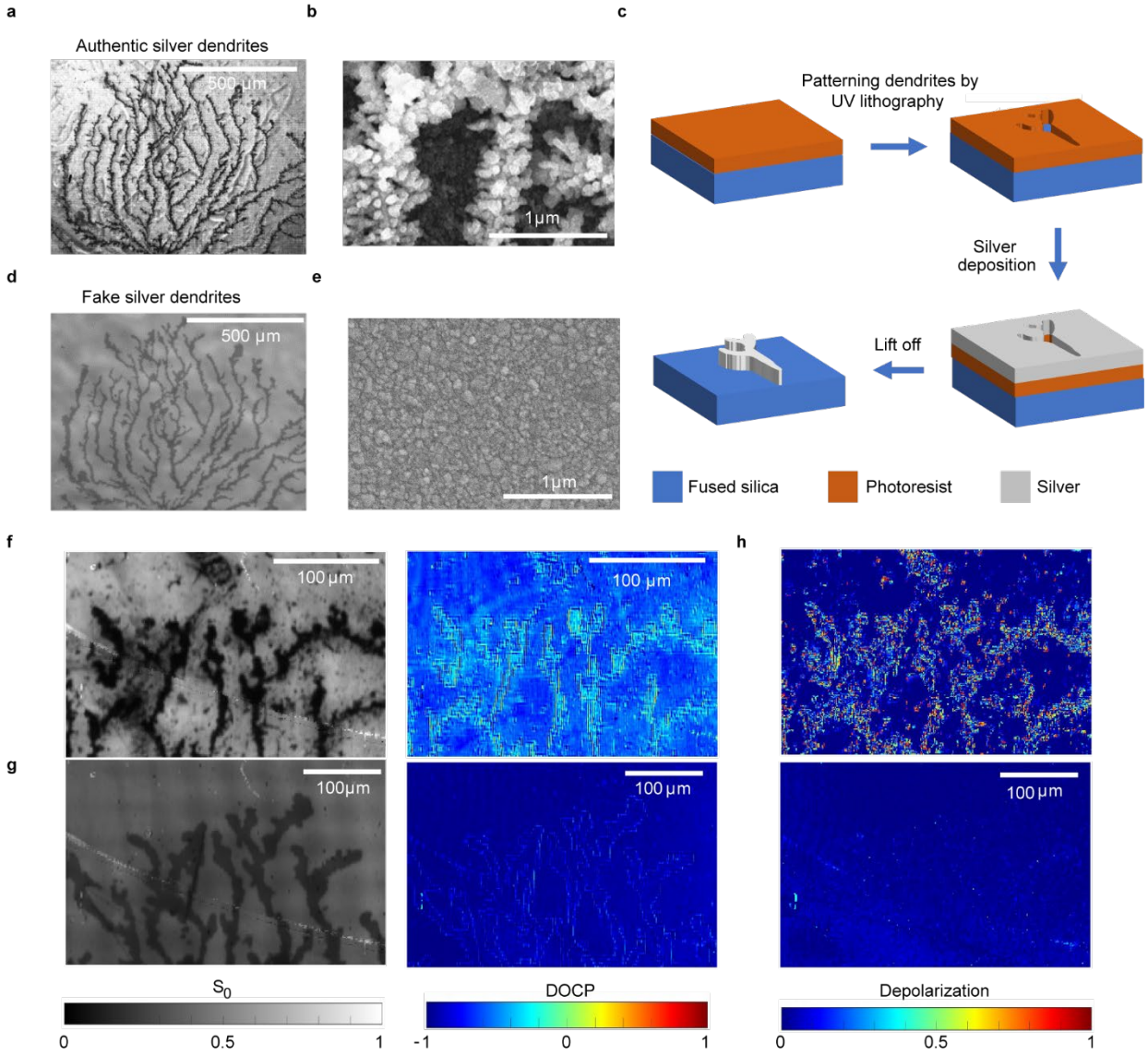


**Figure 23: Characterization of surface morphology in metallic structures.**
**a**, Zoomed-in image (×2) of grown silver dendrites. **b**, Scanning electron microscopic (SEM) image of grown silver dendrites. **c**, Fabrication flow chart of faking silver dendrites by UV lithography and metal deposition. A thin layer of Photoresist was spin-coated on the fused silica substrate, the faked silver dendrite was then patterned using a UV laser writer, followed by Ag thermal deposition and lift-off. **d**, Photo, and microscopic picture of fake silver dendrites. A sample photo is taken with white paper under the substrate to increase contrast. **e**, SEM image of duplicated silver dendrites by UV lithography. **f, g**, Full Stokes polarization image of grown silver dendrites and fake silver dendrites under red color input respectively. **h**, Depolarization image of grown and fake silver dendrites derived from their MM image under red color input. Figure adapted with permission from reference [6]

### *Imaging of biological samples: discovery of birefringence in honeybee wings*

Polarization information of biological samples has been extensively studied in biology and clinical research. For example, the linear birefringence was applied as an importance index for diagnosing cancer[22] and studying the composition of potato starch[23]. Moreover, linear or circular dichroism was used to study insects' behaviors and

communications [24, 25], and plants' growth [26]. The polarization vision of honeybees has been studied extensively[27], and scientists have observed various shreds of evidence suggesting the use of polarization information by honeybees in their social activities [28]. Here, we investigated the wing of a honeybee using the Meta-MMM and revealed an optically birefringent structure on the honeybee wings for the first time in literature to our best knowledge. Figure 24a shows the zoomed-in images (×4 for the middle and ×28 for the right) of the hind wing of a honeybee, which is composed of wing cells and veins. We took MM images of one of the vein joints in transmission mode with red light illumination. Figure 24b shows the DOCP images of vein joints under LP input light with polarization axis along 0°,45°,90°, and 135°, respectively. When the input light is polarized along or orthogonal to the vein joints, the transmitted light shows a small DOCP. When input light is ~±45° with respect to the vein joints, the transmitted light exhibits a DOCP value of ~±0.2. Such DOCP response suggests the tissues connecting bee wing cells and the vein joints have linear birefringence. The optical fast axis of vein joints is along the joint length direction, as shown by the arrows drawn in Fig. 24c. The linear retardance value of the vein joints extracted from the MM is shown in Fig. 24d, revealing an advanced phase difference of the vein joints with a value of ~0.17π to 0.19π along the vein joints compared to the wing cells. We also obtained DOCP and extracted linear retardance images in green color and observed similar phenomena as described above, where linear retardance of ~0.17π to 0.19π exists mainly at cells connecting the vein joints and wing cells, revealing a broadband optical birefringence characteristic of the vein joints. Our study suggests that besides polarization vision, Using MMM to study other body parts in bees might be useful for fully understanding how they make use of polarized light. Furthermore, our Meta-MMM could provide ultra-compact and high-speed solutions for obtaining polarization and MM images of other biological samples for tissue analysis, cancer diagnosis, and study of insects, plant growths, etc.

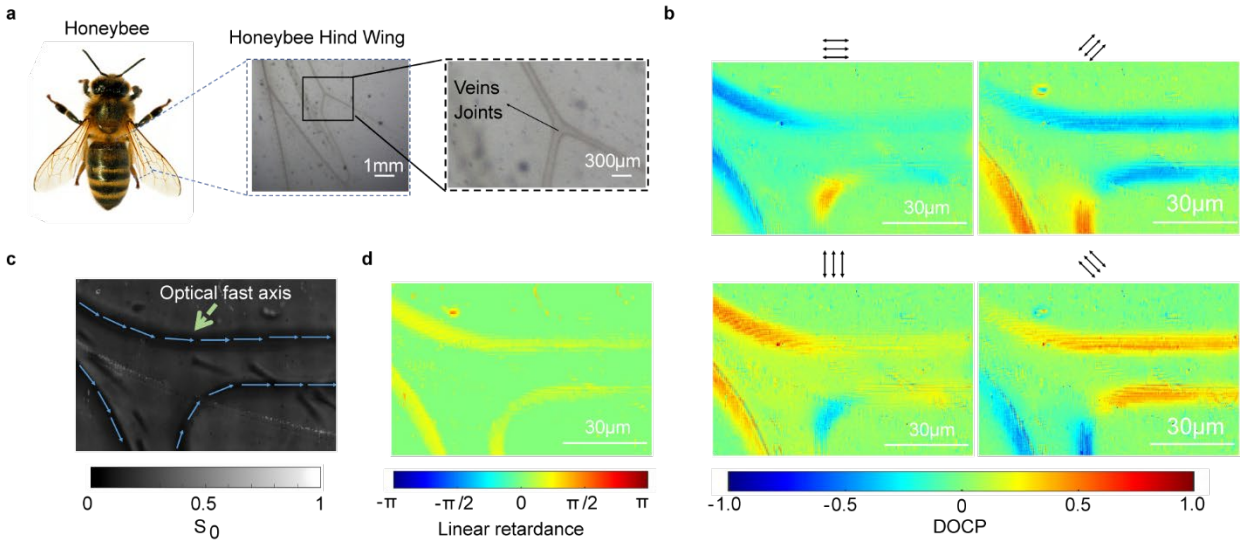


**Figure 24. Full Stokes polarimetric images and Mueller matrix microscopic images of honeybee hind wings. a**, Microscopic image of honeybee hind wing vein joints. **b**, DOCP images of honeybee vein joints with LP input polarized along 0°,45°,90°,135°respectively, polarization images were taken under red light illumination. **c**, Illustration of the optical fast axis of the honeybee wing joints. **d**, Linear retardance extracted from MM of honeybee wing joints under red light illumination. Figure adapted with permission from reference [6]

## 8. Significant Accomplishments and Conclusions:

In task 1 (developing polarimetric imaging systems for autonomous detection), the ASU team has completed the configuration and characterization of a UAV-integrated polarimetric imaging system for collecting preliminary data on the CSP field. The setup has been sent to the Sandia team for field measurement. The developed polarimetric imaging UAV (drone) has been used in Sandia for two field tests so far. We have collected feedback from the field test to improve the system configuration to accommodate practical testing environments and challenges. We used the preliminary results taken from the field test to verify our theoretical model and inspire new ideas.

Meanwhile, we have also demonstrated a full-stokes polarimetric imaging sensor (~60K pixels). The device characterization results show root-mean-square (RMS) errors for Stokes parameters $S_1$ $S_2$ and $S_3$ are all <0.02, which meet the requirement for future field tests. We have finished the fabrication of polarization filter arrays with pixel size 5.6 μm, total area of 4x5 $mm^2$ for full-stokes polarimetric imaging with nanoimprint lithography method and bonded them on CMOS imaging sensors to realize 3 polarimetric imaging sensors. The alignment error between the two metasurfaces is less than 200 nm and the SEM images show reasonably good uniformity. We have completed the device calibration for full-stokes polarimetric imaging measurements and achieved sufficient measurement accuracy (measurement error for all stokes parameters <3% with standard deviation of 2%).

We have completed a polarimetric imaging drone with frame rate 20fps and polarization measurement error <2% (for degree of linear polarization (DOLP) and angle of polarization (AOP))and use it for field tests in Sandia National Solar Thermal Test Facility (NSTTF). We have improved the system performance based on the feedback from the field tests. We are building a new polarimetric imaging drone system with improved performance.

In task 2 (polarimetry-based detection of mirror edge, corner, crack and scratch), the Sandia team collected polarimetry images of heliostat mirrors at Sandia's NSTTF with polarimetric imaging UAV (drone). We have applied polarimetric imaging analysis algorithms on CSP mirror images taken at Sandia National Solar Thermal Test Facility (NSTTF), and the results show obvious improvement of image contrast for mirror edges, corners and cracks for mirror facets compared to conventional imaging sensor, esp. for the situations when it is challenging to identify CSP facets from the background in conventional images. We obtained >90% success rates for the detection of mirror edge/corner and cracks. We have collected polarization images of the heliostats which are suitable for optical error evaluation based on UFACET method during the most recent field test early November 2022. We finished the optical error analysis of the mirrors based on polarimetric images.

In task 3 (polarimetry-based mirror soiling monitoring), we have set up the theoretical model and collected preliminary results in outdoor tests to verify the model and perform mirror soiling detection. We have been able to measure the reflection efficiency of mirrors with different soiling levels with accuracy of ~1% (for soiled mirrors with reflection 90%~100%). We have characterized mirrors with four different soiling samples from other places, e.g., Sandia, Sahara Desert, etc. We have developed the measurement procedures for field tests in CSP plant without affecting the regular operation.

In task 4 (polarimetry-based solar receiver tube monitoring), we have set up a theoretical model for a better understanding of the polarimetry imaging results of the receiver tube. The results show good agreement with experimental results and suggest that visible polarimetric imaging with sunlight and skylight can provide robust imaging contrast for detection of receiver tube defects, such as missing black paints, scratches, deformation (e.g., tube bending), etc. We built a receiver tube array for future investigation and found out that polarimetric imaging can also help to detect liquid on the receiver tube surface, which could help with Melton salt leak detection at high operation temperature.

In Task 5, we have presented our results to other researchers and industry, received feedback from them and discussed potential collaborations with Heliogen, Solar dynamics and Solar services. Besides, we have also perform literature research, interviews and pilot studies to identify potential applications of full-stokes polarization imaging for autonomous vision, PV plant inspection, bubble detection and nanostructure/nanomaterial characterization.

## 9. Path Forward:

The proposed project plan was carried out mostly the same as the one listed in the SOPO and PMP submitted at the beginning of the project and we have completed most EOP goals. Our technology is ready for tests in real CSP plants. We will continue discussing with companies of interests to explore the path for practical world application and commercialization process.

## 10. Products:

1) Tian, M., Rafique, M. Z. E., Chidambaranathan, K., Brost, R., Small, D., Novick, D., ... & Yao, Y. (2025). A Polarimetry-based Field-deployable Non-interruptive Mirror Soiling Detection Method. *arXiv preprint arXiv:2501.01643*. Submitted to Solar Energy.

2) Zuo, Jiawei, Ashutosh Bangalore Aravinda Babu, Mo Tian, Jing Bai, Shinhyuk Choi, Hossain Mansur Resalat Faruque, Sarah Holloway, Michael N. Kozicki, Chao Wang, and Yu Yao. *Advanced Functional Materials* (2024): 2405412.

3) Choi, Shinhyuk, Jiawei Zuo, Nabasindhu Das Yu Yao, and Chao Wang. “Scalable Nanoimprint Manufacturing of Functional Multilayer Metasurface Devices”, *Adv. Funct. Mater.*2024, 2405412.

4) Jiawei Zuo, Jing Bai, Shinhyuk Choi, Ali Basiri, Xiahui Chen, Chao Wang, Yu Yao, “Chip-Integrated metasurface Full-Stokes Polarimetric CMOS Imaging Sensor”, *Light Sci Appl* **12**, 218 (2023).

5) Rafique, Md Zubair Ebne, Hossain Mansur Resalat Faruque, Ahmed Hassan, Mo Tian, Nabasindhu Das, and Yu Yao. “Field Deployable Mirror Soiling Detection Based on Polarimetric Imaging.” In *SolarPACES Conference Proceedings*, vol. 1. 2022.

6) Tian, Mo, Neel Desai, Jing Bai, Randy Brost, Daniel Small, David Novick, Julius Yellowhair, Md Zubair Ebne Rafique, Vishnu Pisharam, and Yu Yao. “Toward Autonomous Field Inspection of CSP Collectors with a Polarimetric Imaging Drone.” In *SolarPACES Conference Proceedings*, vol. 1. 2022.

7) Invited talk: Jiawei Zuo, Jing Bai, Shinhyuk Choi, Ali Barsiri, Xiahui Chen, Chao Wang, YuYao. "Chip-Integrated Full-Stokes Polarimetric Imaging Sensor." *International Conference on Electron, Ion and Photon Beam Technology and Nanofabrication 2022*. EIPBN, 2022.

8) Jiawei Zuo, Jing Bai, Shinhyuk Choi, Xiahui Chen, Chao Wang, YuYao “Chip-Integrated Full-Stokes Polarimetric Imaging Sensor”, *CLEO: Applications and Technology*. Optical Society of America, 2022

9) Jing Bai, Jiawei Zuo, Yu Yao, “Mid-Infrared Chip-Integrated Full-Stokes Polarimeter Array Based on Plasmonic Metasurfaces” *CLEO: Applications and Technology*. Optical Society of America, 2022

10) Bai, Jing, and Yu Yao. "Highly efficient anisotropic chiral plasmonic metamaterials for polarization conversion and detection." *ACS nano* 15.9 (2021): 14263-14274.

## 11. Project team and roles:

PI: Yu Yao (ASU), Project management.
Co PI: Chao Wang (ASU), scalable nanomanufacturing
Co PI: Julius Yellowhair / Randy Brost (Sandia): field tests and industry exploration
Other contributors from ASU: Mo Tian, Jiawei Zuo, Jing Bai, Md Zubair Rafique, Vishnu Pisharam, Kolappan Chidambaranathan, Neal Desai, Shinhyuk Choi, Robert Stirling,
Other contributors from Sandia: Dan Small, David Novick.

## References:

[1] M. Papaelias, L. Cheng, M. Kogia, A. Mohimi, V. Kappatos, C. Selcuk*, et al.*, "Inspection and structural health monitoring techniques for concentrated solar power plants," *Renewable Energy,* vol. 85, pp. 1178-1191, 2016.

[2] J. Zuo, J. Bai, S. Choi, A. Basiri, X. Chen, C. Wang*, et al.*, "Chip-integrated metasurface full-Stokes polarimetric imaging sensor," *Light: Science & Applications,* vol. 12, p. 218, 2023.

[3] A. Basiri, X. Chen, J. Bai, P. Amrollahi, J. Carpenter, Z. Holman*, et al.*, "Nature-inspired chiral metasurfaces for circular polarization detection and full-Stokes polarimetric measurements," vol. 8, pp. 1-11, 2019.

[4] S. Choi, J. Zuo, N. Das, Y. Yao, and C. Wang, "Scalable Nanoimprint Manufacturing of Functional Multilayer Metasurface Devices," *Advanced Functional Materials,* p. 2404852, 2024.

[5] M. Tian, N. Desai, J. Bai, R. Brost, D. Small, D. Novick*, et al.*, "Toward Autonomous Field Inspection of CSP Collectors with a Polarimetric Imaging Drone," in *SolarPACES Conference Proceedings*, 2022.

[6] J. Zuo, A. B. A. Babu, M. Tian, D. Wang, Z. Cen, K. Chidambaranathan*, et al.*, "Metasurface-Based Mueller Matrix Microscope," *Advanced Functional Materials,* vol. 34, p. 2405412, 2024.

[7] V.-C. Su, C. H. Chu, G. Sun, and D. P. J. O. e. Tsai, "Advances in optical metasurfaces: fabrication and applications," vol. 26, pp. 13148-13182, 2018.

[8] J. Bai and Y. J. A. n. Yao, "Highly efficient anisotropic chiral plasmonic metamaterials for polarization conversion and detection," vol. 15, pp. 14263-14274, 2021.

[9] E. Arbabi, S. M. Kamali, A. Arbabi, and A. Faraon, "Full-Stokes imaging polarimetry using dielectric metasurfaces," *Acs Photonics,* vol. 5, pp. 3132-3140, 2018.

[10] N. A. Rubin, G. D'Aversa, P. Chevalier, Z. Shi, W. T. Chen, and F. Capasso, "Matrix Fourier optics enables a compact full-Stokes polarization camera," *Science,* vol. 365, 2019.

[11] M. Khorasaninejad, W. Chen, A. Zhu, J. Oh, R. Devlin, D. Rousso*, et al.*, "Multispectral chiral imaging with a metalens," vol. 16, pp. 4595-4600, 2016.

[12] S.-Y. Lu and R. A. J. J. A. Chipman, "Interpretation of Mueller matrices based on polar decomposition," vol. 13, pp. 1106-1113, 1996.

[13] Y. Socol, O. Abramson, A. Gedanken, Y. Meshorer, L. Berenstein, and A. J. L. Zaban, "Suspensive electrode formation in pulsed sonoelectrochemical synthesis of silver nanoparticles," vol. 18, pp. 4736-4740, 2002.
[14] Z. Zhao, N. Chamele, M. Kozicki, Y. Yao, and C. J. J. o. M. C. C. Wang, "Photochemical synthesis of dendritic silver nano-particles for anti-counterfeiting," vol. 7, pp. 6099-6104, 2019.
[15] M. R. Majidi, S. Ghaderi, K. Asadpour-Zeynali, H. J. M. S. Dastangoo, and E. C, "Synthesis of dendritic silver nanostructures supported by graphene nanosheets and its application for highly sensitive detection of diazepam," vol. 57, pp. 257-264, 2015.
[16] Z.-Q. Cheng, Z.-W. Li, J.-H. Xu, R. Yao, Z.-L. Li, S. Liang*, et al.*, "Morphology-controlled fabrication of large-scale dendritic silver nanostructures for catalysis and SERS applications," vol. 14, pp. 1-7, 2019.
[17] Y. Zhou, G. Zhao, J. Bian, X. Tian, X. Cheng, H. Wang*, et al.*, "Multiplexed SERS barcodes for anti-counterfeiting," vol. 12, pp. 28532-28538, 2020.
[18] M. N. J. A. i. P. X. Kozicki, "Information in electrodeposited dendrites," vol. 6, p. 1920846, 2021.
[19] J. Wang, X. Li, Y. Zou, and Y. J. A. O. Sheng, "Mueller matrix imaging of electrospun ultrafine fibers for morphology detection," vol. 58, pp. 3481-3489, 2019.
[20] C. Chen, C. Ross, N. Podraza, C. Wronski, and R. Collins, "Multichannel Mueller matrix analysis of the evolution of the microscopic roughness and texture during ZnO: Al chemical etching," in *Conference Record of the Thirty-first IEEE Photovoltaic Specialists Conference, 2005.*, 2005, pp. 1524-1527.
[21] S. Rezaei, A. Landarani–Isfahani, M. Moghadam, S. Tangestaninejad, V. Mirkhani, and I. J. C. E. J. Mohammadpoor-Baltork, "Development of a novel bi-enzymatic silver dendritic hierarchical nanostructure cascade catalytic system for efficient conversion of starch into gluconic acid," vol. 356, pp. 423-435, 2019.
[22] C. He, H. He, J. Chang, B. Chen, H. Ma, M. J. J. L. S. Booth*, et al.*, "Polarisation optics for biomedical and clinical applications: a review," vol. 10, pp. 1-20, 2021.
[23] A. R. Bobi Olmo, "Study of the starch grains of tubers using Mueller matrix microscopy," 2021.
[24] I. M. Daly, M. J. How, J. C. Partridge, S. E. Temple, N. J. Marshall, T. W. Cronin*, et al.*, "Dynamic polarization vision in mantis shrimps," vol. 7, p. 12140, 2016.
[25] T. W. Cronin, N. Shashar, R. L. Caldwell, J. Marshall, A. G. Cheroske, T.-H. J. I. Chiou*, et al.*, "Polarization vision and its role in biological signaling," vol. 43, pp. 549-558, 2003.
[26] P. P. Shibayev and R. G. J. I. J. B. Pergolizzi, "The effect of circularly polarized light on the growth of plants," vol. 7, pp. 113-117, 2011.
[27] T. Labhart, E. P. J. M. r. Meyer, and technique, "Detectors for polarized skylight in insects: a survey of ommatidial specializations in the dorsal rim area of the compound eye," vol. 47, pp. 368-379, 1999.
[28] W. Edrich and O. J. J. o. c. p. von Heiversen, "Polarized light orientation of the honey bee: the minimum visual angle," vol. 109, pp. 309-314, 1976.